Predict-then-Optimize for Seaport Power-Logistics Scheduling: Generalization across Varying Tasks Stream

Chuanqing Pu^a, Feilong Fan^a, Nengling Tai^a, Yan Xu^b, Wentao Huang^c, Honglin Wen^{c,d}

^aCollege of Smart Energy, Shanghai Jiao Tong University, Shanghai, 201100, China
 ^bSchool of Electrical and Electronic Engineering, Nanyang Technological University, Singapore
 ^cSchool of Electrical Engineering, Shanghai Jiao Tong University, Shanghai, 200240, China
 ^dDyson School of Design Engineering, Imperial College London, London, United Kingdom

Abstract

Power–logistics scheduling in modern seaports typically follow a predict-then-optimize pipeline. To enhance the decision quality of forecasts, decision-focused learning has been proposed, which aligns the training of forecasting models with downstream decision outcomes. However, this end-to-end design inherently restricts the value of forecasting models to only a specific task structure, and thus generalize poorly to evolving tasks induced by varying seaport vessel arrivals. We address this gap with a decision-focused continual learning framework that adapts online to a stream of scheduling tasks. Specifically, we introduce Fisher information based regularization to enhance cross-task generalization by preserving parameters critical to prior tasks. A differentiable convex surrogate is also developed to stabilize gradient backpropagation. The proposed approach enables learning a decision-aligned forecasting model across a varying tasks stream with a sustainable long-term computational burden. Experiments calibrated to the Jurong Port demonstrate superior decision performance and generalization over existing methods with reduced computational cost. Keywords: Forecasting, decision-focused learning, seaport power-logistics systems, predict-then-optimize, multi-task generalization

1. Introduction

With the accelerated electrification of logistics operations, modern seaports are progressively transforming into power–logistics coupled systems (PLS) characterized by high renewable penetration and flexible logistics loads [1]. In this context, extensive research are devoted to enhancing the operational benefits of PLS through advanced forecasting and scheduling techniques [2, 3, 4]. Concretely, forecasting models capture the stochastic dynamics of net load demand and electricity prices, while PLS schedulers leverage these forecasts to co-optimize energy procurement and logistics operations. This sequential workflow can

be formulated as a *predict-then-optimize* pipeline [5] that mirror real-world industrial practices in seaport PLS operations.

In prevailing predict—then—optimize pipelines, forecasting models are typically trained to minimize statistical losses (e.g. mean squared error, MSE), as shown in Fig. 1(a). However, the decision quality achieved through downstream optimization depends not only on the statistically pointwise accuracy but also on the direction of bias and the temporal structure of the forecast errors [6]. For instance, when a PLS operator forecasts the day-ahead net-load profile, overestimation may lead to excessive energy procurement and trigger downward regulation costs, whereas underestimation causes real-time shortages that trigger upward regulation [7]. The regulation cost is inherently asymmetric under different imbalance settlement mechanisms and also coupled with the day-ahead price profile. These asymmetric and nonlinear effects of forecast errors on scheduling are poorly captured by symmetric, linear statistical losses such as MSE.

To address this misalignment, decision-focused learning (DFL) instead evaluates the decision quality of forecasts through their impact on the downstream optimization tasks [8]. As depicted in Fig. 1(b), DFL integrates forecasting and optimization in an end-to-end pipeline and trains the forecasting model directly by the decision-related loss. Recent work further refines DFL for power system applications by deriving task-aware losses and differentiable solvers that facilitate stable end-to-end training. These studies have established an effective learning paradigm for enhancing decision-making benefits in various power system contexts, including unit commitment [9, 10], economic dispatch [12, 13, 14], cost-oriented renewable-energy forecasting and trading [15, 16, 17], energy-storage arbitrage [18, 19], and multi-energy scheduling [20].

However, this end-to-end learning paradigm inherently confines the forecasting model's decision quality to a fixed and predetermined optimization task. In contrast, PLS scheduling tasks are continuously evolving due to varying vessel arrivals, since logistics decisions must be made conditional on vessel arrivals as exogenous parameters [7]. Each new arrival configuration introduces a distinct task instance characterized by different numbers of vessels, cargo profiles, and time-coupled constraints. Although these tasks share similar high-level formulations, they differ in the dimensions of decision variables and the geometry of feasible regions. As a result, the ground-truth objectives and loss landscapes of DFL is correspondingly varying across different configurations. This constitutes the fundamental distinction between PLS operation and conventional DFL settings in power systems.

Motivated by this nature, this paper investigates the key question that *How can a forecasting model be trained to generalize and remain decision-effective across an evolving stream of tasks?* Recent work explores multi-task and multi-objective DFL variants, in which forecasting models are trained to minimize the average loss across a predefined set of tasks or objectives [21, 22]. Another line of work pretrains a surrogate network to capture the joint effect of forecasts and exogenous task parameters on operational cost [23]. Although these offline extensions improve cross-task generalization, they presuppose prior knowledge of possible task structures and increases the demand for large and diverse offline datasets. This limitation is amplified in

PLS operations, where unforeseen configurations arise continually due to the dynamic and unpredictable nature of global vessel arrivals [1].

Online continual learning thus provides a computationally sustainable solution for long-term adaptation, yet two challenges still remain: i) How to retain the decision quality of forecasts on past tasks? Due to the computational intensity of DFL, cumulative retraining or replaying past tasks leads to prohibitive computational costs under bounded model and memory capacity [24]. ii) How to ensure the computationally feasibility? The mixed-integer coupling of logistics decisions often yields discontinuous gradients in backpropagation of DFL and destabilizes end-to-end training [25].

To address these challenges, we firstly reformulate conventional static DFL into a decision-focused continual learning (DFCL) paradigm, as illustrated in Fig. 1(c). DFCL sequentially learns over a stream of PLS tasks in an online manner. Inspired by the concept of Elastic Weight Consolidation (EWC) [26], we derive a regularization method that constrains updates to parameters critical for past decision mappings. This design allows the forecasting model to preserve decision-effective information accumulated from previous tasks while adapting to new task conditions. Compared to replay-based continual learning that require frequent re-optimization over historical data [27], the proposed approach preserves cross-task generalization without repeated evaluations of the embedded optimization layer. Moreover, the embedded non-differentiability of the PLS scheduling problem is also addressed through a differentiable surrogate that locally convexifies the problem when back-propagating gradients. The remained convex structure can be efficiently differentiated through implicit differentiation [25]. In the case studies calibrated to the Jurong Port, it is observed that conventional task-specific DFL settings indeed fail to sustain decision performance when sequentially adapted to task streams. The proposed DFCL consistently outperforms statistic-based learning (SBL) and existing DFL methods. The main contributions of this work are summarized as follows:

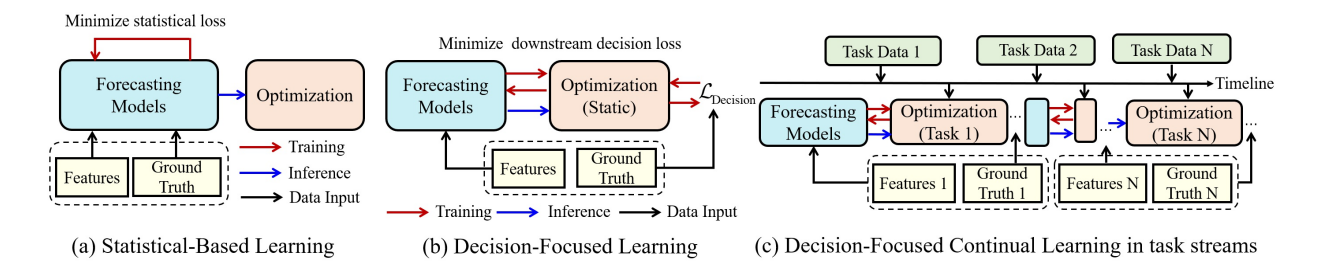


Figure 1: Illustration of different learning paradigms for predict-then-optimize pipelines.

- A novel task-adaptive predict-then-optimize framework is proposed for PLS scheduling, which enables continually learning a decision-aligned forecasting model while preserving generalization over an unbounded task stream.
- A Fisher information based regularization method is proposed to enhance the cross-task generaliza-

tion in the task stream. This avoids the explosive growth of computational overhead from frequent retraining of past tasks.

An end-to-end learning pipeline is developed, which employs a differentiable surrogate to convexify the
embedded mixed-integer PLS scheduling problem and stabilize gradient back-propagation by implicit
differentiation.

The rest of this paper is organized as follows. Section 2 presents the predict-then-optimize pipeline of PLS. Section 3 formulates the DFCL problem for the PLS task stream. Section 4 introduces the differentiable end-to-end learning pipeline to implement DFCL. Section 5 reports the experimental setup and results. Section 6 concludes the paper.

2. Predict-then-Optimize Pipeline in PLS

This study considers a seaport PLS operating as a price-taking industrial consumer in an electricity market with single-price imbalance settlement. The PLS comprises photovoltaics (PV) generation, an energy storage system (ESS), uncontrollable residential loads and a logistics subsystem including vessel berthing, quay-crane operations, and shore power supply.

The operation of the seaport PLS is modeled as a sequential predict-then-optimize pipeline that mirrors real industrial practice. It consists of three consecutive stages: (i) Day-ahead forecasting (S_1), (ii) Day-ahead scheduling and bidding (S_2), and (iii) Real-time scheduling (S_3). In the predict-then-optimize pipeline, S_1 forecasts two types of exogenous input for the following stages over a planning horizon of T time intervals: the market electricity price $\hat{\pi} \in \mathbb{R}^T$, and the net load $\hat{\mathbf{p}} \in \mathbb{R}^T$, defined as the uncontrollable demand minus PV generation within the port area. The predicted $\hat{\pi}$ and $\hat{\mathbf{p}}$ serve as the basis for S_2 , where the PLS determines its day-ahead energy bid $\mathbf{P}_b \in \mathbb{R}^T$ and logistics scheduling plan. The day-ahead schedule specifies the charging/discharging power of the ESS ($\mathbf{P}_{\mathrm{ES.ch}}, \mathbf{P}_{\mathrm{ES.dch}} \in \mathbb{R}^T$), the shore-power supply $\mathbf{P}_s \in \mathbb{R}^T$ to berthed vessels and the quay-crane power $\mathbf{P}_{\mathrm{QC}} \in \mathbb{R}^T$, together with binary logistics indicators \mathbf{V} that represent vessel-berth assignment decisions. The actual electricity price π and realized net load \mathbf{p} are revealed later in S_3 , where deviations between the day-ahead bid \mathbf{P}_b and realized consumption \mathbf{P}_b' are settled according to imbalance coefficients ρ^+ and ρ^- for up- and down-regulation, respectively.

2.0.1. Day-ahead Forecasting

Let ϕ_p and ϕ_l denote the contextual feature vectors for price and load forecasting, respectively, and θ_p , θ_l the corresponding model parameters. The forecasting models are formulated as

$$\hat{\boldsymbol{\pi}} = g_{\pi}(\boldsymbol{\phi}_{\mathbf{p}}; \boldsymbol{\theta}_{\mathbf{p}}), \quad \hat{\mathbf{p}} = g_{\mathbf{l}}(\boldsymbol{\phi}_{\mathbf{l}}; \boldsymbol{\theta}_{\mathbf{l}}),$$
 (1)

where $g_{\pi}(\cdot)$ and $g_{l}(\cdot)$ denote the forecasting functions for price and load, respectively. In practice, these functions can be instantiated using various machine learning models.

2.0.2. Day-ahead Scheduling

Given the upstream forecasts $(\hat{\boldsymbol{\pi}}, \hat{\mathbf{p}})$, PLS co-optimizes energy and logistics plans and submits \mathbf{P}_b to the market. At this stage, the optimization problem is parameterized by two types of exogenous parameters: (i) Static parameters $\boldsymbol{\xi}_s$ that remain constant throughout the planning horizon, including ESS capacity, logistics infrastructure and operational limits; and (ii) Dynamic parameters $\boldsymbol{\xi}_d$ that vary over time, such as vessel arrival times, cargo demands, and handling priorities.

Given these parameters, let $\mathcal{X}_{ES}(\boldsymbol{\xi}_s)$ and $\mathcal{X}_{LG}(\boldsymbol{\xi}_s, \boldsymbol{\xi}_d)$ denote the feasible sets of the ESS and logistics subsystems, respectively. Define the decision vector as $\mathbf{x} := [\mathbf{P}_b^\top, \mathbf{P}_b^\top, \mathbf{P}_{ES.ch}^\top, \mathbf{P}_{ES.ch}^\top, \mathbf{P}_{ES.dch}^\top, \mathbf{P}_s^\top, \mathbf{V}^\top]^\top$, the day-ahead scheduling problem can be formulated as

$$\min_{\mathbf{x}} f(\mathbf{P}_{b}, \mathbf{P}'_{b}; \hat{\boldsymbol{\pi}}) = \boldsymbol{\pi}^{\top} \mathbf{P}_{b} + \rho^{+} \boldsymbol{\pi}^{\top} \Delta \mathbf{P}^{+} - \rho^{-} \boldsymbol{\pi}^{\top} \Delta \mathbf{P}^{-}$$
(2a)

s.t.
$$\left[\mathbf{P}_{\mathrm{ES.ch}}^{\top}, \mathbf{P}_{\mathrm{ES.dch}}^{\top}\right]^{\top} \in \mathcal{X}_{\mathrm{ES}}(\boldsymbol{\xi}_s),$$
 (2b)

$$\left[\mathbf{P}_{s}^{\top}, \mathbf{P}_{QC}^{\top}, \mathbf{V}^{\top}, \mathbf{z}(\mathbf{x})\right]^{\top} \in \mathcal{X}_{LG}(\boldsymbol{\xi}_{s}, \boldsymbol{\xi}_{d}), \tag{2c}$$

$$\Delta \mathbf{P}^+, \ \Delta \mathbf{P}^- \ge 0,$$
 (2d)

$$\Delta \mathbf{P}^{+} - \Delta \mathbf{P}^{-} = \mathbf{P}_{b}' - \mathbf{P}_{b}, \tag{2e}$$

$$\mathbf{P}_{b}' = \mathbf{P}_{s} + \mathbf{P}_{QC} - \mathbf{P}_{ES.dch} + \mathbf{P}_{ES.ch} + \hat{\mathbf{p}}, \tag{2f}$$

where the variable $\mathbf{z}(\mathbf{x})$ represents the remaining intermediate variables determined by \mathbf{x} . The first term of (2a) represents the ex-ante cost on the predicted price, and the second and third terms account for penalties associated with deviations from the bid in actual power consumption. (2d) and (2e) are used to linearize the cost function, and (2f) represents the power balance constraint. Detailed formulations of the ESS and logistics feasible sets $\mathcal{X}_{\text{ES}}(\cdot)$ and $\mathcal{X}_{\text{LG}}(\cdot)$ can be found in Appendix Appendix A.

2.0.3. Real-time Scheduling

Real-time scheduling aims to determine the actual power demand of the PLS. Since ESS and logistics operations exhibit strong sequential coupling over the course of a day, their flexibility is best utilized when planned in advance. The shore power supply can still be re-dispatched in real time according to ultra-short-term forecast updates. Given that these forecasts have a very short lead time relative to actual scheduling actions, it is reasonable to approximate them as the ground truth when evaluating the value of decisions [13, 20]. Accordingly, the real-time scheduling can be formulated as the following equivalent problem

$$\min_{\mathbf{P}_{b}'} f(\mathbf{P}_{b}^{*}(\hat{\boldsymbol{\pi}}, \hat{\mathbf{p}}), \mathbf{P}_{b}'; \boldsymbol{\pi}) \tag{3a}$$

s.t.
$$[\mathbf{P}_{s}^{\top}, \mathbf{P}_{QC}^{*\top}, \mathbf{V}^{*\top}]^{\top} \in \mathcal{X}_{LG}(\boldsymbol{\xi}_{s}, \boldsymbol{\xi}_{d}),$$
 (3b)

$$\mathbf{P}_{b}^{'} = \mathbf{P}_{s} + \mathbf{P}_{OC}^{*} - \mathbf{P}_{ES,dch}^{*} + \mathbf{P}_{ES,ch}^{*} + \mathbf{p},$$
 (3c)

where $\mathbf{P}_{\mathrm{b}}^{*}(\hat{\boldsymbol{\pi}}, \hat{\mathbf{p}})$, $\mathbf{P}_{\mathrm{ES.dch}}^{*}$, $\mathbf{P}_{\mathrm{ES.ch}}^{*}$, $\mathbf{P}_{\mathrm{QC}}^{*}$, and \mathbf{V}^{*} are the optimal solutions obtained from (2). The actual net load \mathbf{p} is used in place of the predicted net load $\hat{\mathbf{p}}$ in (3c).

3. Decision-Focused Continual Learning in PLS

3.1. Decision-Focused Learning Formulation

Through the above predict-then-optimize pipeline, the final daily operating cost of PLS can be calculated as $f(\mathbf{P}_{\mathrm{b}}^{*}(\hat{\boldsymbol{\pi}},\hat{\mathbf{p}}),\mathbf{P}_{\mathrm{b}}^{'*}(\hat{\boldsymbol{\pi}},\hat{\mathbf{p}}),\pi)$, where $\mathbf{P}_{\mathrm{b}}^{'*}(\hat{\boldsymbol{\pi}},\hat{\mathbf{p}})$ is the optimal solution of (3) given the day-ahead decisions based on the predictions $\hat{\boldsymbol{\pi}}$ and $\hat{\mathbf{p}}$.

To evaluate the decision-making value of forecasting models, we define the regret function as

$$\mathcal{L}_{\text{reg}}(\hat{\boldsymbol{\pi}}, \boldsymbol{\pi}, \hat{\mathbf{p}}, \mathbf{p}) = f(\mathbf{P}_{b}^{*}(\hat{\boldsymbol{\pi}}, \hat{\mathbf{p}}), \mathbf{P}_{b}^{'*}(\hat{\boldsymbol{\pi}}, \hat{\mathbf{p}}); \boldsymbol{\pi}) - f(\mathbf{P}_{b}^{*}(\boldsymbol{\pi}, \mathbf{p}), \mathbf{P}_{b}^{'*}(\boldsymbol{\pi}, \mathbf{p}); \boldsymbol{\pi}).$$

$$(4)$$

The first term denotes the actual cost incurred when decisions are based on predicted values, and the second term denotes the cost achievable with perfect foresight. The regret therefore measures the additional cost caused by forecast errors.

We define a task au as the specific scheduling configuration parameterized by

$$\tau := \tau(\boldsymbol{\xi}_s, \boldsymbol{\xi}_d) = (\mathcal{X}_{ES}(\boldsymbol{\xi}_s), \ \mathcal{X}_{LG}(\boldsymbol{\xi}_s, \boldsymbol{\xi}_d), \ \mathcal{D}_{\tau}), \tag{5}$$

where \mathcal{D}_{τ} denotes the contextual feature and ground-truth distribution under $(\boldsymbol{\xi}_s, \boldsymbol{\xi}_d)$. For a single task $\tau(\boldsymbol{\xi}_s, \boldsymbol{\xi}_d)$, the objective of DFL is to find the optimal parameters $\boldsymbol{\theta}_p$ and $\boldsymbol{\theta}_l$ that minimize the regret, i.e., to identify the parameters that are most beneficial for the entire predict-then-optimize pipeline. This can be formulated as a tri-level optimization problem:

$$\min_{\boldsymbol{\theta}_{\mathrm{n}},\boldsymbol{\theta}_{\mathrm{l}}} \mathbb{E}_{(\boldsymbol{\phi}_{\mathrm{p}},\boldsymbol{\phi}_{\mathrm{l}},\boldsymbol{\pi},\mathbf{p}) \sim \mathcal{D}_{\tau}} \left[\mathcal{L}_{\mathrm{reg}}(\hat{\boldsymbol{\pi}},\boldsymbol{\pi},\hat{\mathbf{p}},\mathbf{p}) \right]$$
(6a)

s.t.
$$\mathbf{P}_{\mathrm{b}}^{*}(\hat{\boldsymbol{\pi}}, \hat{\mathbf{p}}), \mathbf{P}_{\mathrm{ES,dch}}^{*}, \mathbf{P}_{\mathrm{ES,ch}}^{*}, \mathbf{P}_{\mathrm{QC}}^{*}, \mathbf{V}^{*}$$
 (6b)

$$= \arg\min_{\mathbf{x}} f(\mathbf{P}_{b}, \mathbf{P}'_{b}; \hat{\boldsymbol{\pi}}) \quad \text{s.t. (2b)} - (2f), \tag{6c}$$

$$\mathbf{P}_{b}^{'*}(\hat{\boldsymbol{\pi}}, \hat{\mathbf{p}}), \mathbf{P}_{s}^{*} = \arg\min_{\mathbf{P}_{b}^{'}, \mathbf{P}_{s}} f(\mathbf{P}_{b}^{*}(\hat{\boldsymbol{\pi}}, \hat{\mathbf{p}}), \mathbf{P}_{b}^{'}; \boldsymbol{\pi})$$
(6d)

s.t.
$$(3b) - (3c)$$
.

The expectation in (6a) is taken over the joint distribution of contextual features and ground-truth values. This formulation defines DFL under a single task setting. However, since the PLS configuration evolves dynamically with vessel arrival conditions, the following section extends this formulation to a continual learning setting on a stream of tasks.

3.2. Decision-Focused Continual Learning for PLS Task Stream

Fig. 2 schematically illustrates the principle of DFCL. As shown in the left panel, SBL and DFL tasks often correspond to distinct loss landscapes, indicated by the different shaded regions in this figure. Statistical loss (e.g., MSE) typically yields symmetric cross-sections, whereas regret loss may tend to be more irregular. Consequently, different loss landscape determines the divergence between the model representations learned by SBL and those optimized for DFL. Specifically, parameters trained under SBL, denoted as θ_{SBL}^* , often converge to the statistical optimum but not necessarily to a low-regret region for DFL. Similarly, the distinction between DFL and DFCL can also be explained through their loss landscapes, as shown in the right panel. Starting from θ_{init} , stochastic gradient descent (SGD) sequentially learns Task A and Task B. DFL updates the parameters to the low-regret region of Task B, resulting in θ_{DFL}^* , but deviates from the low-regret region of Task A. DFCL instead retains Task A information and guides the parameters toward θ_{DFCL}^* , which lies in the overlap of low-regret regions for both tasks.

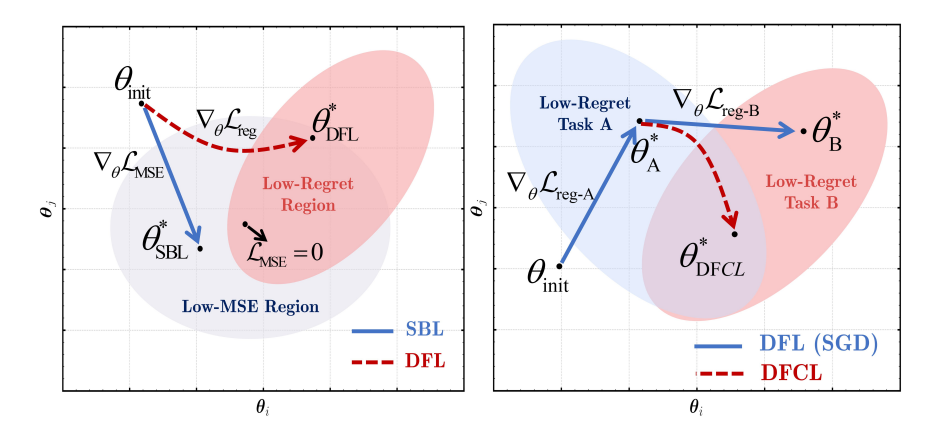


Figure 2: Illustration of the loss landscapes for SBL vs. DFL (left) and DFL vs. DFCL (right). The x-axes and y-axes represent two dimensions of the parameter space, and the differently colored regions denote low-loss areas of distinct loss landscapes. The arrows indicate different learning trajectories.

Given a task stream $\{\tau_1, \tau_2, \dots, \tau_K\}$, the ideal objective of DFCL is to learn the forecasting model parameters $\Theta = \{\theta_p, \theta_l\}$ that minimize the total regret across all encountered tasks. However, since DFCL can only learn one task at a time rather than performing multi-task learning, it must minimize the regret loss of the current task while preventing significant performance degradation in previous tasks, without storing or replaying task data.

For a new task τ_k , the formulation of DFCL can be described as a maximum likelihood estimation problem

$$\min_{\Theta} \quad p(\Theta|\mathcal{D}_{1:k}) = p(\mathcal{D}_k|\Theta) \cdot p(\Theta|\mathcal{D}_{1:k-1}), \tag{7}$$

where \mathcal{D}_k is the dataset for task τ_k , and $\mathcal{D}_{1:k-1}$ represents the datasets of all previous tasks. Taking the

negative logarithm of (7) yields

$$\min_{\Theta} -\log p(\mathcal{D}_{k}|\Theta) - \log p(\Theta|\mathcal{D}_{1:k-1})$$

$$\iff \min_{\Theta} \left\{ \mathbb{E} \left[\mathcal{L}_{\text{reg}}(\hat{\boldsymbol{\pi}}, \boldsymbol{\pi}, \hat{\mathbf{p}}, \mathbf{p}; \Theta) | \mathcal{D}_{k} \right] - \log p(\Theta|\mathcal{D}_{1:k-1}) \right\}.$$
(8)

The first term in (8) corresponds to minimizing the regret loss on the current task, while the second term represents maximizing the prior knowledge distilled from previous tasks into the parameter distribution.

Given the posterior $p(\Theta|\mathcal{D}_{1:k-1})$ after tasks $\mathcal{D}_{1:k-1}$, we apply a Laplace approximation [30] to approximate it as a Gaussian distribution

$$p(\Theta|\mathcal{D}_{1:k-1}) \approx \mathcal{N}(\Theta; \Theta_{k-1}^*, \mathbf{P}_{k-1}^{-1}),$$
 (9)

where Θ_{k-1}^* is the optimal parameter obtained after learning task τ_{k-1} , and \mathbf{P}_{k-1} is the precision matrix defined as the Hessian of the negative log-posterior at Θ_{k-1}^* . Substituting (9) into (8), the negative log-posterior can be expressed as

$$-\log p(\Theta|\mathcal{D}_{1:k-1}) = \frac{1}{2} (\Theta - \Theta_{k-1}^*)^{\top} \mathbf{P}_{k-1} (\Theta - \Theta_{k-1}^*)$$
$$+ \frac{d}{2} \log(2\pi) - \frac{1}{2} \log |\mathbf{P}_{k-1}|,$$
(10)

where d is the dimension of Θ . Ignoring the constant terms in (10) and substituting it into the single-sample expectation of (8), the DFCL problem in τ_k can be reformulated as

$$\min_{\boldsymbol{\Theta}} \quad \left\{ \mathbb{E} \left[\mathcal{L}_{\text{reg}}(\hat{\boldsymbol{\pi}}, \boldsymbol{\pi}, \hat{\mathbf{p}}, \mathbf{p}; \boldsymbol{\Theta}) | \mathcal{D}_k \right] + \frac{1}{2} (\boldsymbol{\Theta} - \boldsymbol{\Theta}_{k-1}^*)^\top \mathbf{P}_{k-1} (\boldsymbol{\Theta} - \boldsymbol{\Theta}_{k-1}^*) \right\}.$$
(11)

The objective of DFCL can be regarded as minimizing the regret loss on the current task while preventing forgetting of previous tasks through a quadratic regularization term.

Calculating the precision matrix \mathbf{P}_{k-1} is a crucial step in implementing DFCL. An approximate calculation method is presented here, and the detailed proof of this approximation is provided in Appendix Appendix B to maintain readability. \mathbf{P}_{k-1} can ultimately be approximated by the empirical Fisher information matrix $\hat{\mathbf{F}}_t(\Theta_{k-1}^*)$ by sample averaging:

$$\mathbf{P}_{k-1} = \sum_{t-1}^{k-1} \beta_t \, \widehat{\mathbf{F}}_t(\Theta_{k-1}^*), \tag{12}$$

where β_t is a scaling factor that can be interpreted as the number of samples in task τ_t , and $\hat{\mathbf{F}}_t(\Theta)$ can be estimated by

$$\widehat{\mathbf{F}}_t(\Theta) = \frac{1}{|\mathcal{D}_t|} \sum_{n=1}^{|\mathcal{D}_t|} \nabla_{\Theta} \mathcal{L}_{\text{reg}}(z_n^{(t)}; \Theta) \nabla_{\Theta} \mathcal{L}_{\text{reg}}(z_n^{(t)}; \Theta)^{\top}, \tag{13}$$

where $z_n^{(t)} = (\phi_p, \phi_l, \boldsymbol{\pi}, \mathbf{p})_n^{(t)}$ is the *n*-th sample. Fisher information measures the identifiability of parameters. Larger eigenvalues indicate a greater influence of the corresponding parameters on the observed data, necessitating stronger consolidation during the learning of new tasks to prevent forgetting.

Remark 1: Unlike naive online learning that relies solely on current-task gradients, DFCL consolidates decision-relevant knowledge from past tasks through Fisher Information, thereby achieving continual adaptation without data replay.

Remark 2: DFCL framework is general and can be applied to various forecasting models and task configurations. The key requirement is the ability to compute the gradients of regret loss with respect to the forecasting parameters, which can be achieved through differentiable optimization techniques.

4. Solution Method for DFCL in PLS

Solving the DFCL problem relies on gradient-based optimization, where ensuring end-to-end differentiability is essential to enable automatic differentiation through computation graph. To this end, a complete end-to-end training framework is proposed, as illustrated in Fig. 3, with detailed descriptions provided in the following subsections. The framework consists of three layers: the forecasting layer, the surrogate layer, and the optimization layer. In the forecasting layer, a neural network-based model jointly processes contextual features of price and net load along with dynamic vessel features. In the surrogate layer, since existing differentiable optimization methods do not support direct differentiation through non-convex constrained problems [25], a convexified surrogate model is introduced for the non-convex feasible set of the PLS scheduling problem. This surrogate predicts local variables \mathbf{P}_{QC} and \mathbf{V} based on upstream forecasts and fixes them to ensure that the remaining subproblem is convex. In the optimization layer, the PLS scheduling problem is solved based on the forecasting results and the surrogate model, and the regret loss is computed for backpropagation and calculation of the Fisher information matrix in (13).

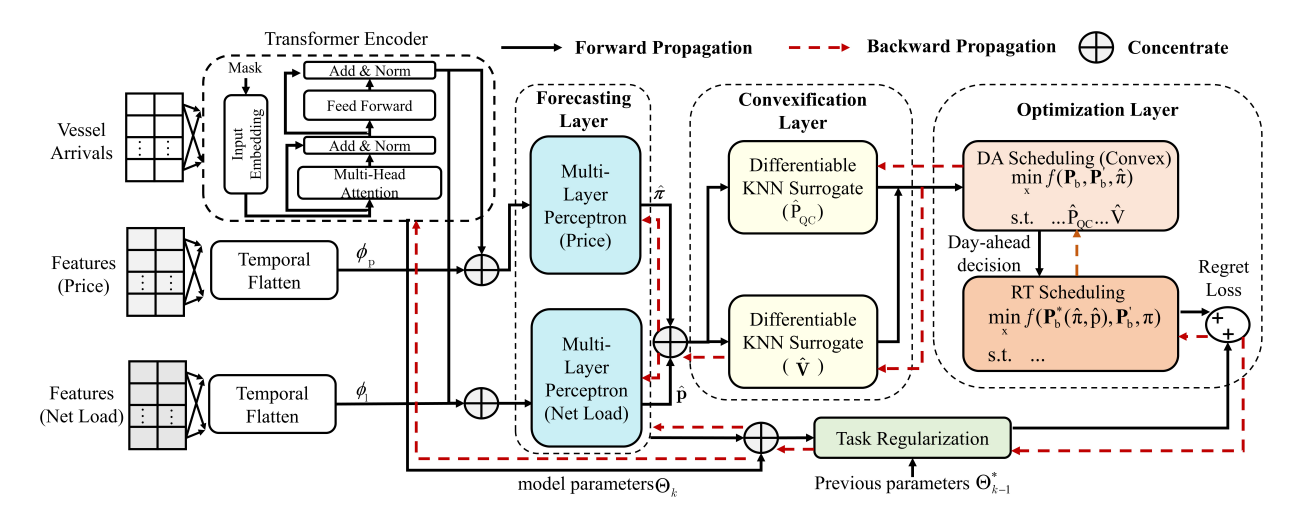


Figure 3: End-to-end training pipeline for DFCL in PLS. Each module represents a differentiable computational unit.

4.1. Forecasting Model

The forecasting model consists of a Transformer Encoder and a Multi-Layer Perceptron (MLP), as shown in Fig. 3. Its mathematical formulation is already provided in (1). Since the number of arriving vessels is variable, the Transformer Encoder is employed to process dynamic vessel-related features $\xi_{\rm d}$ to obtain a fixed-length representation, which is concatenated with static contextual features and passed to the MLP for prediction. Separate Transformer–MLP modules are designed for net load and price forecasting. For net load forecasting, the selected contextual features include historical residential load data from the past 72 hours and one week ago, one-hot encoded timestamp features, and irradiance data. For price forecasting, the chosen contextual features comprise historical electricity prices from the past 72 hours and one week ago, along with one-hot encoded timestamp features.

4.2. Gradient Estimation for PLS Scheduling

4.2.1. Problem Convexification via Surrogate Model

A critical challenge in enabling gradient-based learning for PLS lies in the non-convexity of the embedded optimization problem, which arises primarily from discrete decision variables within the feasible set $\mathcal{X}_{LG}(\boldsymbol{\xi}_s, \boldsymbol{\xi}_d)$ in (2c). These variables govern vessel sequencing, berth allocation, and quay-crane scheduling, leading to a combinatorial structure that prevents direct differentiation through the optimization layer. To enable end-to-end gradient back-propagation, the PLS scheduling problem must therefore be convexified while preserving its operational characteristics.

To this end, we observe that discrete logistics decisions ultimately influence the power–logistics coupling model only through the aggregated load consumption variables ($\mathbf{P}_{\mathrm{QC}}, \mathbf{P}_{\mathrm{s}}$) that appear in the nodal power balance constraints. Hence, the original non-convex feasible region can be relaxed by fixing ($\mathbf{P}_{\mathrm{QC}}, \mathbf{P}_{\mathrm{s}}$) to suitable surrogate values. Since \mathbf{P}_{s} belongs to a convex set when the variable \mathbf{V} is known and \mathbf{P}_{s} is determined in real-time operation, we approximate ($\mathbf{P}_{\mathrm{QC}}, \mathbf{V}$) using a memory-based surrogate model.

A K-Nearest Neighbors (KNN) regression is employed as the surrogate due to its non-parametric nature, which allows adaptive fitting across multiple tasks without catastrophic interference with prior knowledge. This design mitigates overfitting to offline scheduling samples, thereby yielding stable and interpretable gradient estimates. Let upstream forecasts be $\hat{\mathbf{u}} = [\hat{\mathbf{p}}, \hat{\boldsymbol{\pi}}]$, and construct a memory set as

$$\mathcal{M} = \left\{ \left(\mathbf{u}^{(i)}, \mapsto \left(\mathbf{P}_{\mathrm{QC}}^{(i)}, \mathbf{V}^{(i)} \right) \right\}_{i=1}^{M},$$
(14)

for query $\hat{\mathbf{u}}$ in forward-propagation, top-K nearest neighbors are found in memory, and the surrogate is computed as a weighted average of their outputs, as

$$(\hat{\mathbf{P}}_{QC}, \hat{\mathbf{V}})(\hat{\mathbf{u}}) = \sum_{i \in \mathcal{N}_K} w_i(\hat{\mathbf{u}})(\mathbf{P}_{QC}^{(i)}, \mathbf{V}^{(i)}), \tag{15}$$

where \mathcal{N}_K denotes the index set of the K nearest neighbors, and $w_i(\widehat{\mathbf{u}})$ are softmax-based weight. To preserve end-to-end differentiability, the weights ω_i are not chosen by hard truncation (i.e., zeroing all but the K nearest samples), but through a smooth top-k approximation based on cumulative log-sum-exp operations [28]. Detailed formulations of the differentiable top-k operator are provided in the Supplementary Material.

By substituting $(\hat{\mathbf{P}}_{QC}, \hat{\mathbf{V}})$ into the original formulation, the convexified feasible region of (2) can be expressed as

$$\mathcal{X}_{\text{convex}}(\boldsymbol{\xi}_s, \hat{\mathbf{V}}, \hat{\mathbf{P}}_{\text{QC}}) = \mathcal{X}_{\text{ES}}(\boldsymbol{\xi}_s) \cap \{\mathbf{P}_s \mid (2e), (2f), (A.5b)\}. \tag{16}$$

4.2.2. Differentiation of the Regret Loss

The remaining challenge is to compute the gradient of the regret loss \mathcal{L}_{reg} with respect to the forecasting parameters Θ . Let the day-ahead decision be $\mathbf{x}_D^*(\boldsymbol{\eta}) = \left[\mathbf{P}_b^*, \mathbf{P}_{ES.dch}^*, \mathbf{P}_{ES.dch}^*, \mathbf{P}_{QC}^*, \mathbf{V}^*\right]$ from (6c) and the real-time decision is $\mathbf{x}_R^*(\boldsymbol{\eta}, \mathbf{x}_D^*) = \left[\mathbf{P}_b^{'*}, \mathbf{P}_s^*\right]$ from (6d). In the day-ahead problem, the inputs related to Θ include the predicted electricity prices, net load, and the outputs of the surrogate model $(\hat{\mathbf{P}}_{QC}, \hat{\mathbf{V}})$, collectively denoted as $\boldsymbol{\eta} = [\hat{\boldsymbol{\pi}}, \hat{\mathbf{p}}, \hat{\mathbf{P}}_{QC}, \hat{\mathbf{V}}]$. The real-time problem takes the day-ahead decision $\mathbf{x}_D^*(\boldsymbol{\eta})$ as input. According to the chain rule, the gradient w.r.t. any predicted quantity $\boldsymbol{\eta}$ is

$$\frac{d\mathcal{L}_{\text{reg}}}{d\boldsymbol{\eta}} = \frac{\partial \mathcal{L}_{\text{reg}}}{\partial \boldsymbol{\eta}} + \frac{\partial \mathcal{L}_{\text{reg}}}{\partial \mathbf{x}_{D}^{*}} \frac{d\mathbf{x}_{D}^{*}}{d\boldsymbol{\eta}} + \frac{\partial \mathcal{L}_{\text{reg}}}{\partial \mathbf{x}_{R}^{*}} \frac{d\mathbf{x}_{R}^{*}}{d\boldsymbol{\eta}}.$$
(17)

Since \mathcal{L}_{reg} is an explicit function, the partial derivatives $\partial \mathcal{L}_{reg}/\partial \mathbf{x}_{D}^{*}$ and $\partial \mathcal{L}_{reg}/\partial \mathbf{x}_{R}^{*}$ can be computed directly. The remaining challenge is to compute the implicit gradients $\frac{d\mathbf{x}_{D}^{*}}{d\eta}$ and $\frac{d\mathbf{x}_{R}^{*}}{d\eta}$. The following describes how to implicitly compute the gradients of the optimal solution with respect to input parameters from the KKT conditions [29].

Both the day-ahead problem (6c) and the real-time problem (6d) admit a standard conic-QP form

$$\min_{\mathbf{x},\mathbf{s}} \ \frac{1}{2} \mathbf{x}^{\top} \mathbf{P} \mathbf{x} + \mathbf{q}(\boldsymbol{\eta})^{\top} \mathbf{x}$$
 (18a)

s.t.
$$\mathbf{A}(\boldsymbol{\eta})\mathbf{x} + \mathbf{s} = \mathbf{b}(\boldsymbol{\eta}), \quad \mathbf{s} \in \mathcal{K},$$
 (18b)

where the prediction vector enters the linear cost $\mathbf{q}(\eta)$ and the linear maps $\mathbf{A}(\eta)$, $\mathbf{b}(\eta)$. In our setting, $\mathbf{P} = \mathbf{0}$ and $\mathcal{K} = \mathbb{R}^m_+$ (purely linear constraints), i.e., (18) reduces to an LP. When needed to ensure differentiability, we consider a standard Tikhonov regularization $\epsilon \|\mathbf{x}\|^2/2$ (i.e., $\mathbf{P} = \epsilon \mathbf{I}$, $\epsilon > 0$), which leaves the optimizer unchanged in the limit $\epsilon \downarrow 0$ but yields a well-conditioned KKT system.

Let λ be the dual variable of the conic constraint and $\mathbf{s} \in \mathcal{K}$ the slack. The KKT conditions at a

primal-dual solution $(\mathbf{x}^*, \mathbf{s}^*, \boldsymbol{\lambda}^*)$ are

(stationarity)
$$\mathbf{P}\mathbf{x}^* + \mathbf{q}(\boldsymbol{\eta}) + \mathbf{A}(\boldsymbol{\eta})^\top \boldsymbol{\lambda}^* = \mathbf{0},$$
 (19a)

(primal feasibility)
$$\mathbf{A}(\boldsymbol{\eta})\mathbf{x}^* + \mathbf{s}^* - \mathbf{b}(\boldsymbol{\eta}) = \mathbf{0},$$
 (19b)

(dual feasibility)
$$\mathbf{s}^* \in \mathcal{K}, \ \lambda^* \in \mathcal{K}^*,$$
 (19c)

(complementarity)
$$\langle \mathbf{s}^*, \boldsymbol{\lambda}^* \rangle = 0.$$
 (19d)

For $\mathcal{K} = \mathbb{R}^m_+$, (19c)–(19d) reduce to $\mathbf{s}^* \geq 0$, $\boldsymbol{\lambda}^* \geq 0$, and componentwise to $s_i^* \lambda_i^* = 0$. Denote $\mathbf{S} := \operatorname{diag}(\mathbf{s}^*)$ and $\boldsymbol{\Lambda} := \operatorname{diag}(\boldsymbol{\lambda}^*)$. Define the residual mapping $\mathbf{H}(\mathbf{z}, \boldsymbol{\eta}) = \mathbf{0}$ with $\mathbf{z} := (\mathbf{x}, \mathbf{s}, \boldsymbol{\lambda})$ by stacking (19a)–(19b) and a differentiable surrogate for complementarity (e.g., $\mathbf{S}\boldsymbol{\lambda} = \mathbf{0}$ on the active set). Linearizing \mathbf{H} around $(\mathbf{z}^*, \boldsymbol{\eta})$ gives

$$\underbrace{\mathbf{K}}_{:= \partial_{\mathbf{z}} \mathbf{H}(\mathbf{z}^*, \boldsymbol{\eta})} d\mathbf{z} = - \underbrace{\partial_{\boldsymbol{\eta}} \mathbf{H}(\mathbf{z}^*, \boldsymbol{\eta})}_{=: \mathbf{J}_n} d\boldsymbol{\eta}. \tag{20}$$

Under standard regularity, K is nonsingular on the pertinent subspace and hence

$$\frac{d\mathbf{z}^*}{d\boldsymbol{\eta}} = -\mathbf{K}^{-1}\mathbf{J}_{\eta}. \tag{21}$$

The solution of (21) contains the sensitivities of all primal and dual variables. We only need the primal part $\frac{d\mathbf{x}^*}{d\boldsymbol{\eta}}$ for the chain rule (17). For the LP/QP with a non-negative-orthant cone, the Jacobian **K** takes the explicit block form

$$\mathbf{K} = \begin{bmatrix} \mathbf{P} & \mathbf{0} & \mathbf{A}^{\top} \\ \mathbf{A} & \mathbf{I} & \mathbf{0} \\ \mathbf{0} & \mathbf{\Lambda} & \mathbf{S} \end{bmatrix}, \qquad \mathbf{J}_{\eta} = \begin{bmatrix} \partial_{\eta} \mathbf{q} + (\partial_{\eta} \mathbf{A})^{\top} \boldsymbol{\lambda}^{*} \\ \partial_{\eta} \mathbf{A} \mathbf{x}^{*} - \partial_{\eta} \mathbf{b} \\ \mathbf{0} \end{bmatrix}. \tag{22}$$

Here, $\mathbf{A}, \mathbf{b}, \mathbf{q}$ are evaluated at $(\mathbf{x}^*, \boldsymbol{\eta})$ and we suppress the $\boldsymbol{\eta}$ -dependence for readability. The derivatives $\partial_{\boldsymbol{\eta}} \mathbf{A}$, $\partial_{\boldsymbol{\eta}} \mathbf{b}$, and $\partial_{\boldsymbol{\eta}} \mathbf{q}$ are straightforward to compute from the problem data. The sensitivity (21) can be calculated by solving the linear system (20) using the block structure of \mathbf{K} for efficiency.

5. Case Study

5.1. Experimental Setup

5.1.1. Purpose

The case study is designed to answer three questions: Q1: Does DFL effectively reduce costs compared with SBL in PLS applications? Q2: Do the performance of a DFL model trained on a single task degrade when directly generalized to different tasks? Q3: Can the proposed DFCL method mitigate performance degradation in continual learning? The following subsections 5.2-5.4 correspond to answering these three questions, respectively. Besides the conclusive results presented below, further experimental details can be found in the Supplementary Material.

5.1.2. PLS Data Configuration

The experimental data are based on real operational records from Jurong Port in Singapore, including vessel arrival schedules and shore power usage. The port is equipped with ten quay cranes (70 TEU/h, 0.32 MW each), a total berth length of 800 m, and a 5 MW/3 h battery ESS (efficiency 0.9). For day-ahead bidding, imbalance penalty factors are set to $\rho^+ = 1.8$ for upward deviation and $\rho^- = 0.5$ for downward deviation.

5.1.3. Forecasting Datasets

The PV generation dataset was compiled from historical measurements in PES Region 10 of East England, spanning the period from September 2020 to January 2024, and supplemented with meteorological variables obtained from the DWD Center. The corresponding electricity price dataset was collected from the UK day-ahead market over the same time horizon. Both datasets are publicly accessible in [31]. The residential load dataset was obtained from Zone 1 of the GEFCom2014 competition [32] and was temporally aligned with the PV and price datasets to ensure consistency in seasonal effects. The synthesized dataset has been scaled to match the actual scale of the port operations.

5.1.4. Task Settings

Six task scenarios are constructed to simulate online continual learning in PLS. To ensure a fair comparison, each task k shares the same datasets for net load and electricity prices, denoted as $\mathcal{D}_{1}^{(k)} = \{(\phi_{1}^{(n)}, \mathbf{p}^{(n)})\}_{n=1}^{N} \cup \boldsymbol{\xi}_{d}^{(k)}$ and $\mathcal{D}_{p}^{(k)} = \{(\phi_{p}^{(n)}, \boldsymbol{\pi}^{(n)})\}_{n=1}^{N} \cup \boldsymbol{\xi}_{d}^{(k)}$, but features different vessel arrival conditions. Since vessel arrivals involve multiple types of information, key statistical features are extracted for each scenario and summarized in Table 1, with complete details provided in the Supplementary Material. To ensure a robust evaluation of generalization performance, each task scenario includes 402 days of training data and 400 days of testing data.

Table 1: Vessel Arrival Information and Summary Statistics of All Tasks

Task	# Ships	# Int Ships	Arr.	Dep.	Base Pwr	Chg Dem	Chg Max	Cargo	Len.	Max Wait
1	9	3	5 ± 4.95	15 ± 6.04	2.22 ± 1.20	5.33 ± 5.24	1.03 ± 1.03	1433.89 ± 827.21	128.22 ± 37.15	5.00 ± 0
2	9	1	7 ± 4.58	16 ± 4.56	2.56 ± 0.73	6.00 ± 6.14	1.35 ± 1.51	1021.22 ± 714.82	133.78 ± 28.38	5.00 ± 0
3	9	1	9 ± 5.09	19 ± 4.33	2.78 ± 1.09	2.56 ± 4.48	0.53 ± 0.85	1480.11 ± 858.95	134.89 ± 31.31	5.00 ± 0
4	11	3	8 ± 6.67	19 ± 7.75	2.91 ± 1.14	2.00 ± 4.47	0.37 ± 0.83	1416.55 ± 929.75	141.27 ± 29.48	5.00 ± 0
5	9	2	8 ± 6.62	18 ± 8.46	2.44 ± 1.33	0.00 ± 0.00	0.00 ± 0.00	1213.44 ± 855.35	150.44 ± 42.17	5.00 ± 0
6	9	2	8 ± 6.91	19 ± 8.75	2.78 ± 0.97	5.22 ± 6.30	0.94 ± 1.20	952.22 ± 436.25	147.78 ± 39.97	5.00 ± 0

Abbreviations:# Ships = Number of Ships; #Int Ships = Number of Initial In-Port Ships; Arr. = Average Arrival Time; Dep. = Average Departure Time; Base Pwr = Average Base Power Load; Chg Dem = Average Charge Power Demand; Chg Max = Average Charge Power Max; Cargo = Average Cargo Volume; Len. = Average Ship Length; Max Wait = Average Maximum Waiting Time.

5.2. Results of DFL vs. SBL

To evaluate the potential of DFL in reducing operational costs, we compare DFL with several baseline methods on Task 1 as a representative case. The baselines include the SBL approach, the DFL-[14] method that uses warm-start and heuristic strategies for gradient-free optimization of the forecasting model, and the DFL-[23] method that employs a neural network surrogate to approximate the differentiation optimizer. All DFL methods use the same neural network architecture, hyperparameter, and early-stop settings on the Task 1 training set. The performance metrics on the test set are summarized in Table 2.

Method	MAE	MAE	Cost	Regret	Δ	Regret
	(Load)	(Price)	(\$)	(\$)	(%)	(%)
SBL	2.08	13.83	71451.64	3305.85	/	4.85
DFL-[14]	2.17	13.92	71347.43	3201.65	3.15	4.70
DFL-[23]	2.23	27.36	71447.11	3301.32	0.14	4.84
DFL^*	2.25	14.22	71252.49	3106.71	6.02	4.56

Table 2: Performance comparison of different methods.

From Table 2, all variants of DFL reduce the total operating cost relative to SBL, with the proposed method achieving the lowest cost. This improvement is notable given the small differences in net load and price MAE across methods. The regret values further illustrate the performance gap, with the proposed DFL method exhibiting the lowest regret of \$3,106.71 (4.56%), compared to \$3,305.85 (4.85%) for SBL. The gradient-free DFL-[14] delivers limited gains due to its search strategy, while the surrogate-based DFL-[23] suffers from overfitting of gradient estimates, degrading forecast quality and suppressing regret reduction. By contrast, the proposed model-free surrogate provides stable decision gradients even under non-convex and discrete scheduling, enabling more effective parameter updates.

5.3. Results of DFL in Continually Arriving Tasks

To evaluate the performance degradation of a single DFL model under task evolution, we first train the forecasting model using the proposed DFL method on Task1 for 200 epochs and then directly deploy it on the test sets of Tasks 2 to Task 6 without retraining. Fig. 4 presents heat maps of the loss distribution for all test samples across the different tasks. The performance gap Gap(%) is defined as

$$\operatorname{Gap}_{i}(\%) = \frac{\mathbb{E}_{\mathcal{D}_{i}}(\mathcal{L}_{\operatorname{reg}}(\Theta_{1}^{*})) - \mathbb{E}_{\mathcal{D}_{i}}(\mathcal{L}_{\operatorname{reg}}(\Theta_{i}^{*}))}{\mathbb{E}_{\mathcal{D}_{i}}(\mathcal{L}_{\operatorname{reg}}(\Theta_{i}^{*}))} \times 100\%, \tag{23}$$

where $\mathbb{E}_{\mathcal{D}_i}(\mathcal{L}_{reg}(\Theta_1^*))$ denotes the regret of the model trained on Task 1 when evaluated on the test set of Task i, and $\mathbb{E}_{\mathcal{D}_i}(\mathcal{L}_{reg}(\Theta_i^*))$ is the regret of a model trained specifically on Task i.

^{*} denotes the proposed method in this paper.

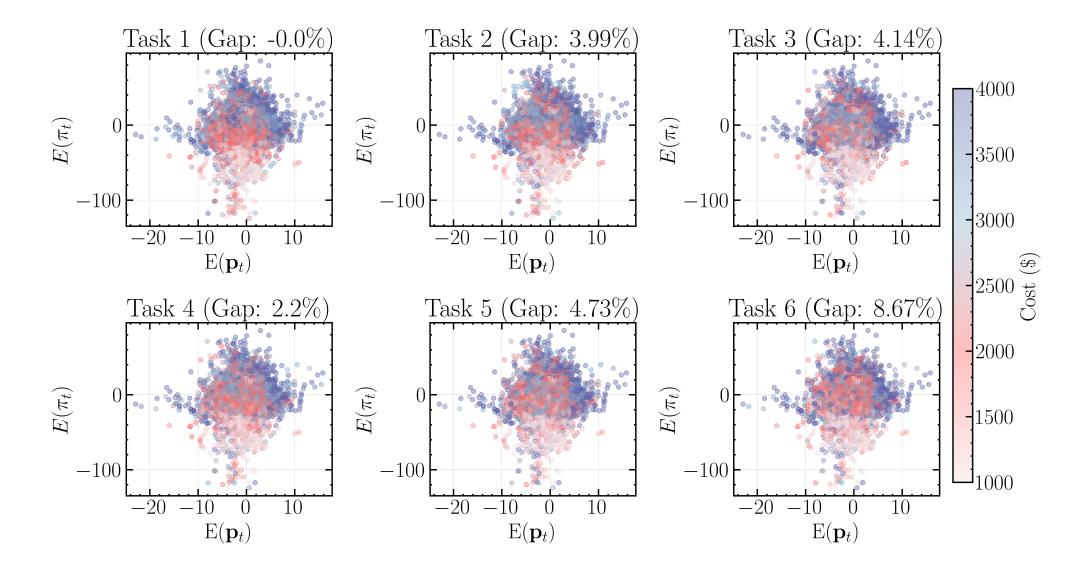


Figure 4: Loss heat maps of a DFL model trained on Task 1 and evaluated on Tasks 1 to 6. The x-axis represents the load forecast error (actual minus predicted), while the y-axis represents the price forecast error. The color intensity indicates the regret value, with colder colors representing higher regret.

Two empirical regularities are observed. First, regret tends to be lower near the center of each heat map, yet many off-center points also exhibit low regret. This indicates that operating cost is not determined solely by forecast error magnitude, which helps explain why DFL can outperform SBL. Second, the loss landscapes differ across tasks, which means that optimal performance on one task does not guarantee optimality on others. A single DFL model trained on Task 1 shows performance degradation ranging from 2.20% to 8.67% on Tasks 2 to 6, as measured by Gap(%).

5.4. Performance Evaluation of DFCL

The aforementioned performance degradation highlights the need for continual learning to adapt to evolving tasks. We evaluate the proposed DFCL method against four baselines: (i) SBL, which retrains the forecasting models from scratch for each task; (ii) DFL (Adam), which continually fine-tunes the DFL model with the Adam optimizer but without any forgetting mitigation; (iii) DFCL (Adam-F), a naïve continual variant that freezes all layers except the last during fine-tuning to preserve prior knowledge; and (iv) the proposed DFCL (EWC). All methods are trained sequentially on Tasks 1–6 under the same neural network architecture and hyperparameters. After completing Task k, we evaluate on the test sets of Tasks 1 through k and report the average MAE of net load and price forecasts, the cumulative regret, the regret ratio (RR), and a forgetting measure (FM) that quantifies performance loss on earlier tasks after learning later ones. The regret ratio is defined as

$$RR_k(\%) = \frac{\sum_{i=1}^k \mathbb{E}_{\mathcal{D}_i}(\mathcal{L}_{reg}(\Theta_k^*))}{\sum_{i=1}^k \mathbb{E}_{\mathcal{D}_i}(f(\cdot; \Theta_k^*)) - \sum_{i=1}^k \mathbb{E}_{\mathcal{D}_i}(\mathcal{L}_{reg}(\Theta_k^*))},$$
(24)

that is, RR_k measures the ratio of cumulative regret to the cumulative optimal cost over the first k tasks. FM evaluates how much performance on earlier tasks deteriorates after learning new ones. For the k-th task, FM is defined as

$$FM_k = \frac{1}{k-1} \sum_{j=1}^{k-1} \left[\max_{i < k} \mathbb{E}_{\mathcal{D}_i} \left(\mathcal{L}_{\text{reg}}(\Theta_j^*) \right) - \mathbb{E}_{\mathcal{D}_j} \left(\mathcal{L}_{\text{reg}}(\Theta_k^*) \right) \right], \tag{25}$$

that is, the average gap between the best historical performance and the current performance on all previous tasks.

After continually learning the first k tasks (k = 1, ..., 6), the average performance on all previously learned tasks is summarized in Table 3. The regret trajectories for Tasks 1–5 across sequential training from Task 1 to Task 6, along with the overall average regret trend, are shown in Fig. 5.

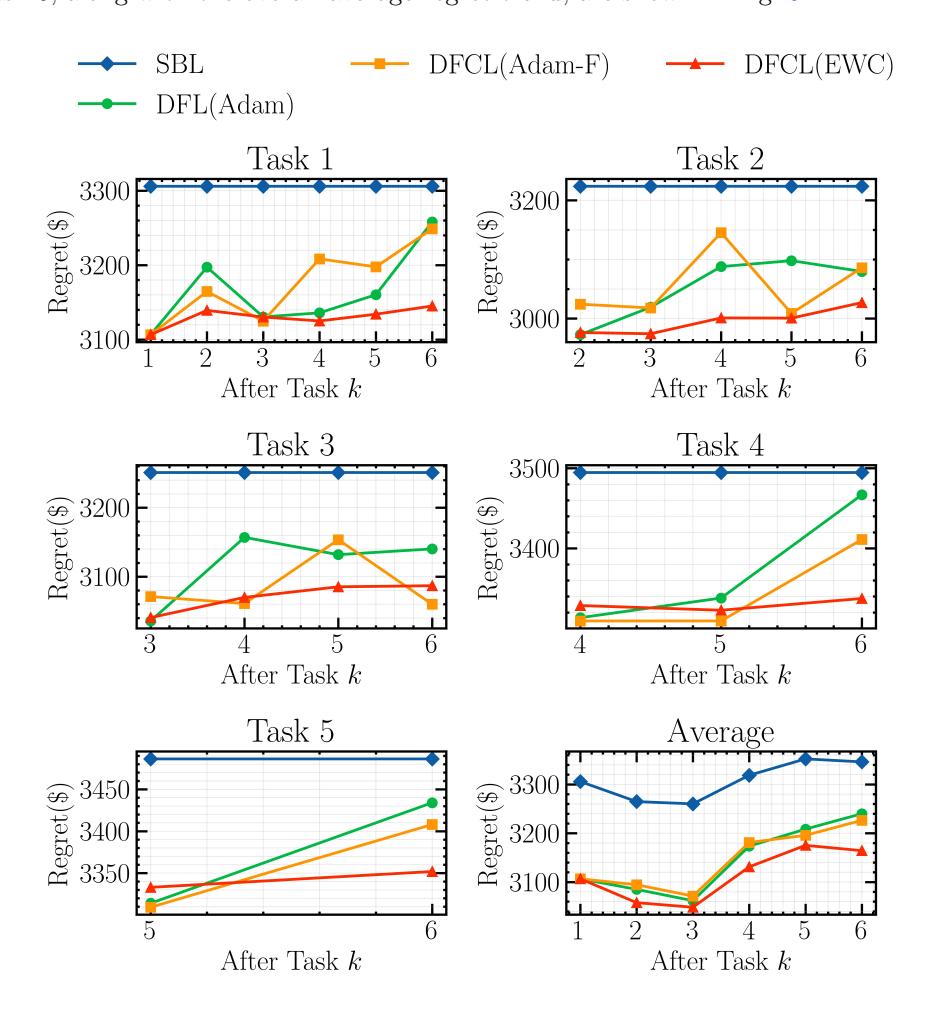


Figure 5: Regret trends on Tasks 1 to 5 and average regret across all tasks after learning each task.

From Table 3 and Fig. 5, the proposed DFCL (EWC) achieves the lowest average regret and regret ratio after training each task and shows the most stable trend over the task streams. By contrast, DFL (Adam)

exhibits pronounced forgetting during continual learning. Relative to DFL (Adam), DFCL (EWC) reduces cumulative regret by up to 2.5% and the forgetting measure by up to 27.7% after completing 6 tasks. This demonstrates the effectiveness of the EWC regularization in promoting cross-task generalization. DFCL (Adam–F) offers slight gains when consecutive tasks have similar ground truth (Tasks 5 and 6), but its forgetting measure is marginally higher on Tasks 2–4, suggesting that freezing layers alone is insufficient to prevent forgetting. Another notable finding is that SBL records the highest regret but the lowest forecast errors across all tasks, consistent with its objective of minimizing statistical error rather than decision loss. This also suggests that DFL confers an inherent degree of cross-task generalization, as illustrated by the overlapping low-regret regions in the schematic loss landscapes of Fig. 2.

Table 3: Performance comparison of different methods in continual learning

		After 7	Γask 1				After 7	Task 2			After Task 3				
Method	$\overline{\mathrm{MAE}_{\mathrm{Lo}}}$	$_{ m id}{ m MAE}_{ m Pric}$	e Regret	RR	FM	$\overline{\mathrm{MAE_{Loa}}}$	$_{ m d}{ m MAE}_{ m Pric}$	Regret	RR	FM	$\overline{\mathrm{MAE_{Los}}}$	$_{ m ad}{ m MAE}_{ m Price}$	Regret	RR	FM
DFL(Task-wise)	2.25	14.22	3106.71	4.56%	0	2.25	14.53	3035.65	4.47%	0	2.24	15.03	3036.60	4.45%	0
SBL	2.08	13.83	3305.85	4.85%	0	2.08	13.83	3264.83	4.81%	0	2.08	13.83	3260.20	4.78%	0
$\mathrm{DFL}(\mathrm{Adam})$	2.25	14.22	3106.71	4.56%	0	2.27	14.14	3085.03	4.54%	91	2.21	14.59	3061.86	4.49%	110
DFCL(Adam-F)	2.25	14.22	3106.71	4.56%	0	2.30	13.90	3094.49	4.56%	58	2.21	14.00	3071.34	4.50%	107
$\mathrm{DFCL}(\mathrm{EWC})$	2.25	14.22	3106.71	4.56%	0 0	2.20	13.85	3057.84	4.50%	33	2.26	14.11	3048.45	4.47%	88
		After 7	Γask 4				After 7	ask 5				After T	ask 6		
Method	$\mathrm{MAE}_{\mathrm{Lo}}$	$_{ m id}{ m MAE}_{ m Pric}$	e Regret	RR	FM	$\mathrm{MAE}_{\mathrm{Loa}}$	$_{ m d}{ m MAE}_{ m Pric}$	_e Regret	RR	\overline{FM}	MAE_{Los}	$_{ m ad}{ m MAE}_{ m Pric}$	Regret	RR	FM
DFL(Task-wise)	2.22	15.44	3103.36	4.59%	0	2.21	15.92	3144.23	4.68%	0	2.21	16.39	3125.79	4.68%	0
SBL	2.08	13.83	3318.80	4.91%	0	2.08	13.83	3352.31	4.99%	0	2.08	13.83	3346.18	5.01%	0
DFL(Adam)	2.20	14.13	3173.62	4.70%	162	2.18	14.15	3208.45	4.77%	217	2.22	15.11	3240.01	4.85%	311
DFCL(Adam-F)	2.15	14.19	3181.07	4.71%	174	2.17	14.10	3195.76	4.75%	203	2.14	14.15	3226.42	4.83%	278
DFCL(EWC)	2.26	14.21	3131.21	4.63%	101	2.19	14.15	3175.21	4.72%	171	2.20	13.98	3164.40	4.73%	225

5.5. Computational Cost Analysis

Additionally, the computational cost of DFCL is compared against the decision-focused multi-task learning (DFMTL) [21] and task-wise DFL under a continual learning setting. The cumulative training times are reported in Fig. 6. For DFMTL, training time grows non-linearly as tasks accumulate, since new task data are merged with all previous data for joint retraining. Task-wise DFL trains a new model from scratch for each incoming task, yielding slightly higher training time than DFL and a memory footprint that increases linearly with the number of tasks. In contrast, DFCL shows a relatively stable training time as tasks accumulate, due to its regularization-based incremental updates.

6. Conclusion

This work addresses the task-generalization challenge of decision-focused forecasting in the sequential task stream of PLS scheduling. The proposed DFCL framework eliminates the need to retrain a bespoke

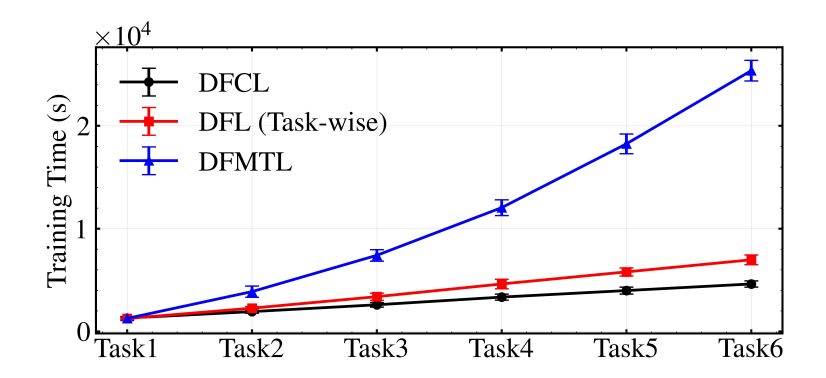


Figure 6: Training time comparison of different methods in continual learning setting.

model for each new task. Across sequences of tasks with varying operational parameters, DFCL consistently enhances decision quality and cross-task generalization compared with naïve Adam-based continual learning, while markedly reducing the computational cost relative to task-wise DFL and multi-task retraining. Rather than providing a one-shot solution that addresses a fixed set of tasks, the proposed framework continuously adapts to evolving task conditions. This offers a practical and efficient approach for seaports to maintain high-quality scheduling decisions amid changing operational contexts. Future research could explore the theoretical underpinnings of task relatedness in DFCL to deepen understanding and broaden applicability to other predict-and-optimize domains.

References

- [1] S. Fang, Y. Wang, B. Gou, and Y. Xu, "Toward future green maritime transportation: An overview of seaport microgrids and all-electric ships," *IEEE Trans. Veh. Technol.*, vol. 69, no. 1, pp. 207–219, 2019.
- [2] Y. Lu, S. Fang, T. Niu, G. Chen, and R. Liao, "Optimal energy-logistics dispatch for seaport green vehicles: Leveraging reversible solid oxide cell energy system for sustainable energy," *IEEE Trans. Ind.* Appl., early access, 2025.
- [3] Y. Zhou, Y. Li, W. Huang, S. Chen, H. Zang, and N. Tai, "Collaborative scheduling of seaport integrated energy, logistics, and vessels: A bi-level Nash-Stackelberg-Nash game approach," *Appl. Energy*, vol. 400, Art. no. 126598, 2025.
- [4] Y. Huang, W. Huang, R. Li, T. Huang, C. Li, and N. Tai, "An adaptive MARL large model for dispatch strategy generation in logistics-energy spatiotemporal coordination of container seaports," *IEEE Trans.* Smart Grid, early access, 2025.
- [5] A. N. Elmachtoub and P. Grigas, "Smart "predict, then optimize"," Manage. Sci., vol. 68, no. 1, pp. 9–26, 2022.

- [6] H. Zhang, R. Li, Q. Du, J. Tao, S. Pineda, G. Kariniotakis, S. Camal, C. B. Monroc, M. Sun, C. Wan, et al., "Decision-focused learning for power system decision-making under uncertainty," *IEEE Trans. Power Syst.*, early access, 2025.
- [7] F. Fan, C. Pu, N. Tai, J. Luo, Z. Chen, and X. Zhang, "Distributed stochastic operation of low-carbon port energy-logistics systems via learning to warm-start," *IEEE Trans. Ind. Appl.*, early access, 2025.
- [8] J. Mandi, J. Kotary, S. Berden, M. Mulamba, V. Bucarey, T. Guns, and F. Fioretto, "Decision-focused learning: Foundations, state of the art, benchmark and future opportunities," J. Artif. Intell. Res., vol. 80, pp. 1623–1701, 2024.
- [9] Y. Zhang, M. Jia, H. Wen, Y. Bian, and Y. Shi, "Toward value-oriented renewable energy forecasting: An iterative learning approach," *IEEE Trans. Smart Grid*, early access, 2024.
- [10] X. Chen, Y. Yang, Y. Liu, and L. Wu, "Feature-driven economic improvement for network-constrained unit commitment: A closed-loop predict-and-optimize framework," *IEEE Trans. Power Syst.*, vol. 37, no. 4, pp. 3104–3118, 2021.
- [11] R. Xie, Y. Chen, and P. Pinson, "Predict-and-optimize robust unit commitment with statistical guarantees via weight combination," *IEEE Trans. Power Syst.*, early access, pp. 1–15, 2025, doi: 10.1109/T-PWRS.2025.3613360.
- [12] J. Han, L. Yan, and Z. Li, "A task-based day-ahead load forecasting model for stochastic economic dispatch," *IEEE Trans. Power Syst.*, vol. 36, no. 6, pp. 5294–5304, 2021.
- [13] C. Lu, W. Jiang, and C. Wu, "Effective end-to-end learning framework for economic dispatch," IEEE Trans. Netw. Sci. Eng., vol. 9, no. 4, pp. 2673–2683, 2022.
- [14] J. Yu, C. Pu, Z. Dou, C. Zhang, J. Li, and F. Fan, "End-to-end forecasting towards economic operation of microgrid using derivative-free learning," in *Proc. IEEE Sustain. Power Energy Conf. (iSPEC)*, 2024, pp. 399–403.
- [15] T. Carriere and G. Kariniotakis, "An integrated approach for value-oriented energy forecasting and data-driven decision-making application to renewable energy trading," *IEEE Trans. Smart Grid*, vol. 10, no. 6, pp. 6933–6944, 2019.
- [16] A. Stratigakos, S. Camal, A. Michiorri, and G. Kariniotakis, "Prescriptive trees for integrated forecasting and optimization applied in trading of renewable energy," *IEEE Trans. Power Syst.*, vol. 37, no. 6, pp. 4696–4708, 2022.

- [17] C. Zhao, C. Wan, and Y. Song, "Cost-oriented prediction intervals: On bridging the gap between forecasting and decision," *IEEE Trans. Power Syst.*, vol. 37, no. 4, pp. 3048–3062, 2021.
- [18] L. Sang, Y. Xu, H. Long, Q. Hu, and H. Sun, "Electricity price prediction for energy storage system arbitrage: A decision-focused approach," *IEEE Trans. Smart Grid*, vol. 13, no. 4, pp. 2822–2832, 2022.
- [19] M. Yi, S. Alghumayjan, and B. Xu, "Perturbed decision-focused learning for modeling strategic energy storage," *IEEE Trans. Smart Grid*, early access, 2025.
- [20] Y. Zhou, Q. Wen, J. Song, X. Cui, and Y. Wang, "Load data valuation in multi-energy systems: An end-to-end approach," *IEEE Trans. Smart Grid*, vol. 15, no. 5, pp. 4564–4575, 2024.
- [21] B. Tang and E. B. Khalil, "Multi-task predict-then-optimize," in *Proc. Int. Conf. Learn. Intell. Optim.*, 2023, pp. 506–522.
- [22] M. H. Dinh, J. Kotary, and F. Fioretto, "End-to-end learning for fair multiobjective optimization under uncertainty," arXiv preprint arXiv:2402.07772, 2024.
- [23] H. Zhang, R. Li, M. Sun, and T. Fei, "Adaptive decision-objective loss for forecast-then-optimize in power systems," arXiv preprint arXiv:2312.13501, 2023.
- [24] E. Verwimp, G. Hacohen, and T. Tuytelaars, "Same accuracy, twice as fast: Continuous training surpasses retraining from scratch," arXiv preprint arXiv:2502.21147, 2025.
- [25] B. Amos and J. Z. Kolter, "OptNet: Differentiable optimization as a layer in neural networks," in *Proc. Int. Conf. Mach. Learn.*, 2017, pp. 136–145.
- [26] J. Kirkpatrick *et al.*, "Overcoming catastrophic forgetting in neural networks," *Proc. Natl. Acad. Sci. USA*, vol. 114, pp. 3521–3526, 2017.
- [27] F. Zhou and C. Cao, "Overcoming catastrophic forgetting in graph neural networks with experience replay," in *Proc. AAAI Conf. Artif. Intell.*, vol. 35, no. 5, pp. 4714–4722, 2021.
- [28] J. Su, "Softmax Backpropagation: A Smooth Approximation for Top-k Selection," Science Space Blog, Sep. 2024. [Online]. Available: https://spaces.ac.cn/archives/10373
- [29] A. Agrawal, B. Amos, S. Barratt, S. Boyd, S. Diamond, and J. Z. Kolter, "Differentiable convex optimization layers," *Adv. Neural Inf. Process. Syst.*, vol. 32, 2019.
- [30] D. J. C. MacKay, Information Theory, Inference and Learning Algorithms. Cambridge, U.K.: Cambridge Univ. Press, 2003.

- [31] J. Browell, D. van der Meer, H. Kälvegren, S. Haglund, E. Simioni, R. J. Bessa, and Y. Wang, "The hybrid renewable energy forecasting and trading competition 2024," arXiv preprint arXiv:2507.01579, 2025.
- [32] T. Hong, P. Pinson, S. Fan, H. Zareipour, A. Troccoli, and R. J. Hyndman, "Probabilistic energy forecasting: Global energy forecasting competition 2014 and beyond," *Int. J. Forecast.*, vol. 32, no. 3, pp. 896–913, 2016.

Appendix A. The constraints of ESS and logistics system

The constraints (2b) are detailed as follows,

$$\mathbf{DE} = \Delta t \left(\eta_{ch} \mathbf{P}_{ES.ch} - \eta_{dch}^{-1} \mathbf{P}_{ES.dch} \right), \tag{A.1a}$$

$$E_{\min} \mathbf{1}_{T+1} \le \mathbf{E} \le E_{\max} \mathbf{1}_{T+1},\tag{A.1b}$$

$$\mathbf{0} \le \mathbf{P}_{\mathrm{ES.ch}}, \, \mathbf{P}_{\mathrm{ES.dch}} \le P_{\mathrm{ES}}^{\mathrm{max}} \mathbf{1}_T,$$
 (A.1c)

where $\mathbf{E} \in \mathbb{R}^{T+1}$ denotes the remaining energy of the ESS; $\mathbf{P}_{\mathrm{ES.ch}}, \mathbf{P}_{\mathrm{ES.dch}} \in \mathbb{R}^T_{\geq 0}$ are the charging and discharging power, respectively; $\mathbf{D} \in \mathbb{R}^{T \times (T+1)}$ is the first-difference operator with $(\mathbf{D}\mathbf{E})_t = E_t - E_{t-1}$; Δt is the time step; η_{ch} and η_{dch} are the charging and discharging efficiencies; and $E_{\mathrm{min}}, E_{\mathrm{max}}$ are the lower and upper energy limits, respectively; $P_{\mathrm{ES}}^{\mathrm{max}}$ is the maximum charge/discharge power. The constraints (2c) are detailed as follows. The nonlinear constraints in (2c) can be linearized using the big-M method. The details are omitted here for brevity, but interested readers can refer to [7].

Ship Scheduling. Let $t_j^{\text{in}}, t_j^{\text{out}}$ be the berthing and departure times of ship j, and v_{jt} represents an entry of the matrix $\mathbf{V} \in \{0,1\}^{|\mathcal{J}| \times T}$, which indicates whether ship j is at berth at time t. Then

$$t_i^{\text{arr}} \le t_i^{\text{in}} \le T, \quad \forall j,$$
 (A.2a)

$$t_j^{\text{in}} + \frac{N_j}{\Delta T \,\eta_{\text{qc}} C_{\text{qc}}^{\text{max}}} \le t_j^{\text{out}} \le t_j^{\text{in}} + \frac{N_j}{\Delta T \,\eta_{\text{qc}} C_{\text{qc}}^{\text{min}}} \quad \forall j, \tag{A.2b}$$

$$t_{j}^{\text{out}} \leq t_{j}^{\text{max}}, \quad t_{j}^{\text{in}} - t_{j}^{\text{arr}} \leq t_{j}^{\text{wait}} \quad \forall j, \tag{A.2c} \label{eq:A.2c}$$

$$v_{jt} = \mathbf{1} \left\{ t_j^{\text{in}} \le t \le t_j^{\text{out}} \right\}, \quad \forall j, t,$$
(A.2d)

$$v_{jt} \ge v_{j,t+1}, \quad \forall j, t_j^{\text{in}} \le t < T,$$
 (A.2e)

where variable t_j^{arr} is the arrival time of ship j, and parameters $N_j, t_j^{\text{max}}, t_{\text{wait}}^{\text{max}}, \Delta T, \eta_{\text{qc}}, C_{\text{qc}}^{\text{min}}, C_{\text{qc}}^{\text{max}}$ are the cargo volume, the latest departure time, the maximum waiting time, the time step, the quay crane operation efficiency, and the minimum and maximum number of quay cranes that can be assigned to a single ship, respectively.

Quay Crane Assignment. For each time t, let c_{kjt} denote the binary assignment of crane $k \in \mathcal{K}$ to ship j. Then

$$C_{\text{qc}}^{\min} v_{jt} \le \sum_{k \in \mathcal{K}} c_{kjt} \ge C_{\text{qc}}^{\min} v_{jt}, \tag{A.3a}$$

$$\sum_{i \in \mathcal{I}} c_{kjt} \le 1, \quad \forall k, t, \tag{A.3b}$$

$$c_{k+1,jt} + c_{k-1,jt} - c_{kjt} \le 1, \quad \forall j, k, t.$$
 (A.3c)

Berth Assignment. Let b_j be the berth position of ship j and l_j its length. Let $S_i = [b_i, b_i + l_i]$ and $\tau_i = [t_i^{\text{in}}, t_i^{\text{out}}]$ be the spatial and temporal occupation intervals of ship i. Then

$$b_i \ge 0, \quad b_i + l_i \le L_{\text{tot}},$$
 (A.4a)

$$(\mathcal{S}_i \cap \mathcal{S}_j = \emptyset) \lor (\tau_i \cap \tau_j = \emptyset), \quad \forall i \neq j, \tag{A.4b}$$

where $L_{\rm tot}$ is the total length of the berth.

Load and Power Constraints. Define the total number of cranes in operation at time t as $\sigma_t := \mathbf{1}_K^{\top} \mathbf{C}_t \mathbf{1}_J$, where $\mathbf{C}_t \in \{0,1\}^{K \times J}$, where $(\mathbf{C}_t)_{kj} = c_{kjt}$. Stacking across all time periods, then

$$\mathbf{P}_{\mathrm{QC}} = P_{\mathrm{qc}}^{\mathrm{rated}} \begin{bmatrix} \mathbf{1}_{K}^{\top} \mathbf{C}_{1} \mathbf{1}_{J} \\ \vdots \\ \mathbf{1}_{K}^{\top} \mathbf{C}_{T} \mathbf{1}_{J} \end{bmatrix} \in \mathbb{R}^{T}, \tag{A.5a}$$

$$\mathbf{P}_{s} = (\mathbf{P}^{\text{base}} + \mathbf{P}^{\text{chg}}) \odot \mathbf{V}, \tag{A.5b}$$

$$0 \le \mathbf{P}^{\text{chg}} \le \mathbf{P}^{\text{max}} \odot \mathbf{V},\tag{A.5c}$$

$$\mathbf{P}^{\text{chg}}\mathbf{1}_T \ge \mathbf{P}^{\text{dmd}},\tag{A.5d}$$

where parameter $P_{\text{qc}}^{\text{rated}}$, \mathbf{P}^{base} , \mathbf{P}^{max} , $\mathbf{P}^{\text{dmd}} \in \mathbb{R}^{|\mathcal{J}|}$ are the rated power of a single quay crane, the base load vector, the maximum charging power vector, and the total charging demand vector of all ships, respectively. The variable $\mathbf{P}^{\text{chg}} \in \mathbb{R}_{\geq 0}^{|\mathcal{J}| \times T}$ is the charging power matrix of all ships, where each row corresponds to a ship and each column to a time period. The operator \odot denotes the Hadamard product.

Appendix B. Proof of the Approximation of Precision Matrix

The precision matrix \mathbf{P}_{k-1} , defined as the Hessian of the negative log-posterior at Θ_{k-1}^* , can be decomposed as

$$\mathbf{P}_{k-1} = \left[\nabla_{\Theta}^{2} \left(-\log p(\Theta) - \sum_{t=1}^{k-1} \log p(\mathcal{D}_{t} \mid \Theta) \right) \right]_{\Theta_{k-1}^{*}}.$$
 (B.1)

In practice, the prior curvature can be absorbed into a constant quadratic regularizer, leading to the approximation

$$\mathbf{P}_{k-1} \approx \mathbf{H}_{k-1} = \sum_{t=1}^{k-1} \left[\nabla_{\Theta}^2 \left(-\log p(\mathcal{D}_t \mid \Theta) \right) \right]_{\Theta = \Theta_{k-1}^*}.$$
 (B.2)

To further relate the empirical curvature \mathbf{H}_{k-1} to an estimable statistical quantity, we invoke the Fisher identity, which links the expected score covariance to the expected negative Hessian of the log-likelihood.

Lemma 1 (Fisher Identity). Let $p(\mathbf{z} \mid \Theta)$ be a correctly specified statistical model, and assume the usual regularity conditions so that differentiation and integration can be interchanged. Denote $s(\mathbf{z}; \Theta) \triangleq$ $\nabla_{\Theta} \log p(\mathbf{z} \mid \Theta)$. Then

$$\mathbb{E}_{\mathbf{z} \sim p(\cdot \mid \Theta)} [s(\mathbf{z}; \Theta) \, s(\mathbf{z}; \Theta)^{\top}] = - \mathbb{E}_{\mathbf{z} \sim p(\cdot \mid \Theta)} [\nabla_{\Theta}^{2} \log p(\mathbf{z} \mid \Theta)]. \tag{B.3}$$

According to Lemma 1, under standard regularity conditions and a well-specified model, the per-sample Fisher information equals the expected negative Hessian. Writing the dataset log-likelihood as $\log p(\mathcal{D}_t \mid$ Θ) $\approx \sum_{n=1}^{N_t} \log p(z_n^{(t)} \mid \Theta)$ then gives Eq. (12) in the main text, where the Fisher information matrix $\mathbf{F}_t(\Theta)$ is initially defined as

$$\mathbf{F}_{t}(\Theta) \triangleq \mathbb{E}_{z \sim p_{t}(\cdot)} \left[\nabla_{\Theta} \log p(z \mid \Theta) \nabla_{\Theta} \log p(z \mid \Theta)^{\top} \right], \tag{B.4}$$

Since the training objective is $\mathcal{L}_{reg}(z_n^{(t)};\Theta)$, to preserve the Fisher-like curvature property, the Hessian of \mathcal{L}_{reg} is approximated by the outer product of its sample gradients:

$$\widehat{\mathbf{F}}_t(\Theta) = \frac{1}{N_t} \sum_{n=1}^{N_t} \nabla_{\Theta} \ell(z_n^{(t)}; \Theta) \nabla_{\Theta} \ell(z_n^{(t)}; \Theta)^{\top}.$$
(B.5)

where $\ell(z;\Theta)$ is the per-sample loss function.

Appendix C. Differentiable surrogate model with a Soft-Top-k Operator

Notation and Setup

Let the memory feature matrix be $\mathbf{M} \in \mathbb{R}^{N \times D}$ and the associated memory labels be $\mathbf{Y} \in \mathbb{R}^{N \times M \times 24}$; when only one label stream is used (M = 1), we view $\mathbf{Y} \in \mathbb{R}^{N \times 1 \times 24}$. For a mini-batch of queries $\mathbf{Q} \in \mathbb{R}^{B \times D}$, we compute a similarity matrix

$$\mathbf{X} \triangleq \sin(\mathbf{Q}, \mathbf{M}) \in \mathbb{R}^{B \times N},\tag{C.1}$$

where the similarity can be chosen as

cosine:
$$X_{b,i} = \frac{\mathbf{Q}_b}{\|\mathbf{Q}_b\|_2} \cdot \frac{\mathbf{M}_i}{\|\mathbf{M}_i\|_2},$$
 (C.2)

euclidean:
$$X_{b,i} = -\|\mathbf{Q}_b - \mathbf{M}_i\|_2^2,$$
 (C.3)

euclidean:
$$X_{b,i} = -\|\mathbf{Q}_b - \mathbf{M}_i\|_2^2$$
, (C.3)
diff-cosine: $X_{b,i} = \frac{\Delta \mathbf{Q}_b}{\|\Delta \mathbf{Q}_b\|_2} \cdot \frac{\Delta \mathbf{M}_i}{\|\Delta \mathbf{M}_i\|_2}$, $\Delta \mathbf{v} \triangleq [v_2 - v_1, \dots, v_D - v_{D-1}]$. (C.4)

For each query b, denote its similarity vector by $x \in \mathbb{R}^N$ (we suppress b for clarity). Our goal is to produce a soft top-k mask $w \in [0,1]^N$, normalize it to weights

$$\alpha_i = \frac{w_i}{\sum_{j=1}^N w_j + \varepsilon},\tag{C.5}$$

and output a differentiable KNN aggregation

$$\hat{\mathbf{y}} = \sum_{i=1}^{N} \alpha_i \, \mathbf{Y}_i \in \mathbb{R}^{M \times 24} \quad \text{(squeeze to } \mathbb{R}^{24} \text{ if } M = 1\text{)}.$$
 (C.6)

Soft-Top-k as a Smooth Threshold Equation

Define a smooth surrogate of the indicator via a soft step centered at a threshold $\lambda \in \mathbb{R}$:

$$\phi(t) = \left(1 - e^{-|t|}\right) \frac{\operatorname{sign}(t)}{2} + \frac{1}{2} = \begin{cases} 1 - \frac{1}{2}e^{-t}, & t > 0, \\ \frac{1}{2}e^{t}, & t \le 0. \end{cases}$$
(C.7)

Given $x \in \mathbb{R}^N$, the soft-top-k mask is defined by

$$w_i \triangleq \phi(x_i - \lambda^*), \quad \text{where } \lambda^* \text{ satisfies } S(\lambda^*) = k, \quad S(\lambda) \triangleq \sum_{i=1}^N \phi(x_i - \lambda).$$
 (C.8)

Intuitively, increasing λ decreases $S(\lambda)$; hence a unique (or almost unique) solution exists under mild separability.

Sorting and Interval Decomposition. Let $x_{(1)} \leq \cdots \leq x_{(N)}$ be the ascending sort of x, and consider the N half-open intervals

$$\lambda \in [x_{(i)}, x_{(i+1)})$$
 for $i = 1, \dots, N$, with $x_{(N+1)} \triangleq +\infty$.

On the interval $[x_{(i)}, x_{(i+1)}),$

$$x_{(j)} - \lambda \le 0 \ (j \le i), \qquad x_{(j)} - \lambda > 0 \ (j > i),$$

and by (C.7) we obtain

$$S(\lambda) = \sum_{j \le i} \frac{1}{2} e^{x_{(j)} - \lambda} + \sum_{j > i} \left(1 - \frac{1}{2} e^{-(x_{(j)} - \lambda)} \right) = (N - i) + \frac{1}{2} \left(e^{-\lambda} \underbrace{\sum_{j \le i} e^{x_{(j)}}}_{A_i} - e^{\lambda} \underbrace{\sum_{j > i} e^{-x_{(j)}}}_{B_i} \right), \quad (C.9)$$

where we introduced the cumulative exponentials

$$A_i \triangleq \sum_{i \le i} e^{x_{(j)}}, \qquad B_i \triangleq \sum_{i > i} e^{-x_{(j)}}.$$
 (C.10)

Closed-Form Threshold per Interval

Let $y \triangleq e^{\lambda} > 0$ and define $m_i \triangleq N - 1 - i$ and $\Delta_i \triangleq k - m_i$ (note $N - i = m_i + 1$). Setting $S(\lambda) = k$ in (C.9) yields the quadratic equation in y:

$$B_i y^2 + 2\Delta_i y - A_i = 0. (C.11)$$

Proposition 1 (Interval-wise solution). On interval $[x_{(i)}, x_{(i+1)})$, the positive root of (C.11) is

$$y_i^{\star} = \frac{-\Delta_i + \sqrt{\Delta_i^2 + A_i B_i}}{B_i} = \frac{A_i}{\sqrt{\Delta_i^2 + A_i B_i} + \Delta_i}, \qquad \lambda_i^{\star} = \log y_i^{\star}. \tag{C.12}$$

The valid solution must satisfy the interval constraint

$$x_{(i)} \le \lambda_i^{\star} < x_{(i+1)}. \tag{C.13}$$

In practice we scan i = 1, 2, ..., N and select the first λ_i^* that meets (C.13).

Numerically Stable Implementation via Log-Sum-Exp

Directly forming A_i and B_i may cause overflow/underflow. Using the logsumexp trick,

$$\ell_i^{(1)} \triangleq \log A_i = \operatorname{logsumexp}(x_{(1:i)}), \qquad \ell_i^{(2)} \triangleq \log B_i = \operatorname{logsumexp}(-x_{(i+1:N)}),$$
 (C.14)

we compute (cf. (C.12))

$$\lambda_i^{\star} = \ell_i^{(1)} - \log\left(\sqrt{\Delta_i^2 + \exp\left(\ell_i^{(1)} + \ell_i^{(2)}\right)} + \Delta_i\right),$$
 (C.15)

which avoids catastrophic cancellation by evaluating $\sqrt{\Delta_i^2 + A_i B_i} + \Delta_i$ in log-domain. The interval check (C.13) is then performed against the sorted $x_{(i)}$ and $x_{(i+1)}$ (with $x_{(N+1)} = +\infty$). If no valid interval exists (a rare degenerate case), a safe fallback is $w = \mathbf{0}$.

Soft Mask and Final Aggregation

With the chosen λ^* , the per-entry mask follows (C.7):

$$w_{i} = \phi(x_{i} - \lambda^{\star}) = \begin{cases} 1 - \frac{1}{2}e^{-(x_{i} - \lambda^{\star})}, & x_{i} \geq \lambda^{\star}, \\ \frac{1}{2}e^{x_{i} - \lambda^{\star}}, & x_{i} < \lambda^{\star}, \end{cases} \qquad \alpha_{i} = \frac{w_{i}}{\sum_{j=1}^{N} w_{j} + \varepsilon}, \qquad \widehat{\mathbf{y}} = \sum_{i=1}^{N} \alpha_{i} \mathbf{Y}_{i}. \quad (C.16)$$

Properties and Practical Notes

- Differentiability. For any fixed interval index i (i.e., away from ties), λ_i^* in (C.15) is a composition of smooth functions (logsumexp, log, $\sqrt{\cdot}$), hence $w = \phi(x \lambda^*)$ is smooth almost everywhere and backpropagates stably. When similarities are well separated, w saturates towards $\{0,1\}$ and recovers hard top-k behavior.
- Complexity. Sorting costs $O(N \log N)$; prefix/suffix logsumexp scans and interval testing are O(N). The overall cost is $O(N \log N)$ per query.
- Numerical Stability. Evaluate A_i and B_i only via (C.14), and prefer the rationalized form in (C.15) to avoid subtracting close numbers.

Summary

The soft-top-k operator casts "select the k largest" as a smooth thresholding problem $S(\lambda) = k$ with a closed-form interval-wise solution (C.12) computed robustly via (C.15). Plugging this operator into the KNN aggregation (C.16) yields a fully differentiable surrogate of top-k selection that is efficient, numerically stable, and compatible with gradient-based training.

Code Implementation

Base on the soft-top-k operator (Thre-topK) proposed in [28], we implement a differentiable KNN module that includes both the soft-top-k operator and differentiable KNN aggregation. To facilitate understanding and reproduction, the complete code is provided below.

```
def thre_topk(x: torch.Tensor, k: int) -> torch.Tensor:
2
        # x: 1D tensor
3
        x_sort, _ = torch.sort(x)
 4
       lse1 = torch.logcumsumexp(x_sort, dim=0)
       lse2 = torch.logcumsumexp(-x_sort.flip(0), dim=0).flip(0)
5
        lse2 = torch.cat([lse2[1:], torch.tensor([-float('inf')], device=x.device)], dim=0)
6
       m = torch.arange(len(x) - 1, -1, -1, device=x.device).float()
 7
        temp = (k - m) ** 2 + torch.exp(lse1 + lse2)
 8
        x_lamb = lse1 - torch.log(torch.sqrt(temp) + (k - m))
9
10
        x_sort_shift = torch.cat([x_sort[1:], torch.tensor([float('inf')], device=x.device)])
11
        mask = (x_lamb <= x_sort_shift) & (x_lamb >= x_sort)
12
       lamb = x_lamb[mask]
13
        if len(lamb) == 0:
14
           return torch.zeros_like(x)
15
        lamb = lamb[0]
16
        mask = (1 - torch.exp(-torch.abs(x - lamb))) * torch.sign(x - lamb) * 0.5 + 0.5
17
        return mask
18
19
    class DifferentiableKNN(nn.Module):
        def __init__(self, memory_features: torch.Tensor, memory_labels: torch.Tensor, k: int = 5,
        similarity='cosine'):
21
            super().__init__()
            self.k = k
22
23
            self.similarity = similarity
            self.N = memory_features.shape[0]
24
25
            self.D = memory_features.shape[1]
26
            if memory_labels.dim() == 2:
                memory_labels = memory_labels.unsqueeze(1) # (N,1,24)
27
28
                self.label_single_output = True
29
            elif memory_labels.dim() == 3:
30
                self.label_single_output = False
31
32
                raise ValueError("memory_labels must be of shape (N,24) or (N,M,24)")
            self.M = memory_labels.shape[1]
34
            self.register_buffer("memory_features", memory_features)
35
            self.register_buffer("memory_labels", memory_labels)
36
37
        def compute_similarity(self, query: torch.Tensor) -> torch.Tensor:
            if self.similarity == 'cosine':
38
39
                q = F.normalize(query, dim=1); m = F.normalize(self.memory_features, dim=1)
                sim = torch.matmul(q, m.T)
40
41
            elif self.similarity == 'euclidean':
                q = query.unsqueeze(1); m = self.memory_features.unsqueeze(0)
42
                sim = -((q - m) ** 2).sum(dim=2)
43
44
            elif self.similarity == 'diff-cosine':
45
                def diff(x): return x[:, 1:] - x[:, :-1]
                \label{eq:query_features} $q = F.normalize(diff(query), dim=1); m = F.normalize(diff(self.memory_features), dim=1)$
46
47
                sim = torch.matmul(q, m.T)
48
            else:
49
                raise ValueError(f"Unknown similarity metric: {self.similarity}")
50
51
52
        def forward(self, query: torch.Tensor) -> torch.Tensor:
53
            B = query.shape[0]
            sim = self.compute_similarity(query)
54
            soft_masks = torch.stack([thre_topk(sim[i], self.k) for i in range(B)], dim=0)
            weights = soft_masks / (soft_masks.sum(dim=1, keepdim=True) + 1e-8)
56
57
            memory_labels = self.memory_labels.unsqueeze(0).expand(B, -1, -1, -1)
            weights = weights.unsqueeze(2).unsqueeze(3)
58
59
            output = (weights * memory_labels).sum(dim=1)
60
            return output.squeeze(1) if self.label_single_output else output
```

Listing 1: Differentiable KNN with soft-top-k operator.

Appendix D. Detailed Vessel-Arrival Configuration (Supplement to Table 1)

The following long tables report the complete vessel-arrival configuration for each task. They are intended to be archival for reproducibility and to clarify the exact inputs that parameterize the downstream optimization.

Table D.4: Task 1: Vessel-arrival configuration (rows=9)

Arr.	Dep.	Cargo	Min QC	Max QC	Base Pwr	Chg Dem	Chg Max	Len.	Max Wait
0.0	14.0	2866.0	1.0	3.0	4.0	7.0	1.59	148.0	5.0
0.0	9.0	1816.0	1.0	3.0	1.0	11.0	2.5	122.0	5.0
0.0	14.0	913.0	1.0	3.0	1.0	0.0	0.0	164.0	5.0
2.0	10.0	1606.0	1.0	3.0	4.0	11.0	1.375	199.0	5.0
3.0	9.0	493.0	1.0	2.0	2.0	8.0	1.66	95.0	5.0
5.0	15.0	1351.0	1.0	2.0	2.0	11.0	2.16	134.0	5.0
7.0	20.0	746.0	1.0	1.0	2.0	0.0	0.0	102.0	5.0
10.0	22.0	2446.0	1.0	3.0	3.0	0.0	0.0	83.0	5.0
14.0	26.0	668.0	1.0	3.0	1.0	0.0	0.0	107.0	5.0

Table D.5: Task 2: Vessel-arrival configuration (rows=9)

Arr.	Dep.	Cargo	Min QC	Max QC	Base Pwr	Chg Dem	Chg Max	Len.	Max Wait
0.0	14.0	2866.0	1.0	3.0	3.0	12.0	1.36	148.0	5.0
3.0	12.0	606.0	1.0	1.0	3.0	14.0	2.46	143.0	5.0
4.0	10.0	869.0	2.0	3.0	3.0	0.0	0.0	151.0	5.0
6.0	12.0	549.0	1.0	3.0	2.0	0.0	0.0	113.0	5.0
8.0	14.0	846.0	2.0	3.0	2.0	0.0	0.0	121.0	5.0
9.0	17.0	1071.0	2.0	2.0	3.0	13.0	3.33	111.0	5.0
10.0	17.0	931.0	1.0	2.0	3.0	6.0	1.25	145.0	5.0
11.0	24.0	886.0	1.0	1.0	3.0	9.0	3.75	88.0	5.0
15.0	21.0	567.0	1.0	3.0	1.0	0.0	0.0	184.0	5.0

Table D.6: Task 3: Vessel-arrival configuration (rows=9)

Arr.	Dep.	Cargo	Min QC	Max QC	Base Pwr	Chg Dem	Chg Max	Len.	Max Wait
0.0	11.0	2236.0	1.0	3.0	3.0	0.0	0.0	152.0	5.0
3.0	15.0	2446.0	1.0	3.0	1.0	13.0	2.28	188.0	5.0
7.0	19.0	832.0	1.0	2.0	4.0	0.0	0.0	153.0	5.0
9.0	23.0	2866.0	1.0	3.0	4.0	5.0	1.28	153.0	5.0
10.0	20.0	1351.0	1.0	2.0	4.0	0.0	0.0	144.0	5.0
12.0	18.0	1582.0	2.0	4.0	3.0	5.0	1.25	101.0	5.0
13.0	20.0	838.0	2.0	2.0	2.0	0.0	0.0	89.0	5.0
14.0	23.0	497.0	1.0	1.0	2.0	0.0	0.0	124.0	5.0
15.0	25.0	673.0	1.0	3.0	2.0	0.0	0.0	110.0	5.0

Table D.7: Task 4: Vessel-arrival configuration (rows=11)

Arr.	Dep.	Cargo	Min QC	Max QC	Base Pwr	Chg Dem	Chg Max	Len.	Max Wait
0.0	13.0	558.0	1.0	3.0	1.0	0.0	0.0	166.0	5.0
0.0	8.0	1606.0	2.0	3.0	2.0	10.0	2.27	155.0	5.0
0.0	10.0	2026.0	1.0	3.0	2.0	12.0	1.82	169.0	5.0
3.0	9.0	932.0	2.0	4.0	4.0	0.0	0.0	82.0	5.0
6.0	18.0	2446.0	1.0	3.0	4.0	0.0	0.0	178.0	5.0
9.0	19.0	466.0	1.0	3.0	4.0	0.0	0.0	99.0	5.0
10.0	23.0	582.0	1.0	3.0	2.0	0.0	0.0	147.0	5.0
13.0	26.0	2656.0	1.0	3.0	2.0	0.0	0.0	140.0	5.0
15.0	29.0	2866.0	1.0	3.0	3.0	0.0	0.0	153.0	5.0
16.0	28.0	681.0	1.0	2.0	4.0	0.0	0.0	124.0	5.0
17.0	23.0	763.0	2.0	2.0	4.0	0.0	0.0	141.0	5.0

Table D.8: Task 5: Vessel-arrival configuration (rows=9)

Arr.	Dep.	Cargo	Min QC	Max QC	Base Pwr	Chg Dem	Chg Max	Len.	Max Wait
0.0	7.0	931.0	1.0	2.0	1.0	0.0	0.0	83.0	5.0
0.0	7.0	450.0	1.0	1.0	1.0	0.0	0.0	173.0	5.0
1.0	9.0	905.0	2.0	4.0	2.0	0.0	0.0	198.0	5.0

Continued on next page

Table D.8: Task 5: Vessel-arrival configuration (continued)

Arr.	Dep.	Cargo	Min QC	Max QC	Base Pwr	Chg Dem	Chg Max	Len.	Max Wait
4.0	17.0	1771.0	1.0	2.0	4.0	0.0	0.0	151.0	5.0
7.0	20.0	2656.0	1.0	3.0	2.0	0.0	0.0	153.0	5.0
11.0	23.0	2446.0	1.0	3.0	4.0	0.0	0.0	156.0	5.0
14.0	25.0	640.0	1.0	1.0	4.0	0.0	0.0	189.0	5.0
15.0	29.0	516.0	1.0	3.0	1.0	0.0	0.0	171.0	5.0
16.0	25.0	606.0	1.0	1.0	3.0	0.0	0.0	80.0	5.0

Table D.9: Task 6: Vessel-arrival configuration (rows=9)

Arr.	Dep.	Cargo	Min QC	Max QC	Base Pwr	Chg Dem	Chg Max	Len.	Max Wait
0.0	8.0	555.0	1.0	2.0	3.0	0.0	0.0	87.0	5.0
0.0	11.0	921.0	1.0	3.0	2.0	0.0	0.0	172.0	5.0
2.0	8.0	830.0	2.0	3.0	3.0	0.0	0.0	180.0	5.0
6.0	16.0	484.0	1.0	2.0	3.0	0.0	0.0	159.0	5.0
8.0	21.0	886.0	1.0	1.0	1.0	9.0	1.07	160.0	5.0
11.0	21.0	1351.0	1.0	2.0	4.0	13.0	2.36	195.0	5.0
13.0	27.0	1911.0	1.0	2.0	3.0	12.0	2.31	78.0	5.0
17.0	28.0	746.0	1.0	1.0	4.0	0.0	0.0	156.0	5.0
18.0	31.0	886.0	1.0	1.0	2.0	13.0	2.71	143.0	5.0

For clarity, we standardize the column headings across all detailed tables as follows.

- Arr. (arrival_time): scheduled/relative vessel arrival time (hour of day).
- Dep. (max_leave_time): latest allowable departure/leave time (deadline).
- Base Pwr (base_power_load): baseline vessel power load during berthing.
- Chg Dem (charge_power_demand): charging power demand during berthing.
- Chg Max (charge_power_max): the maximum charging power of the vessel.
- Cargo (cargo_volume): cargo volume associated with the vessel.
- Len. (length): vessel length.

- ullet Min QC / Max QC (min_quay_crane/max_quay_crane): the minimum and maximum number of quay cranes required by the vessel.
- Max Wait (max_waiting_time): upper bound on waiting time before service starts.

Appendix E. Additional Experimental Results

This section provides additional experimental results that complement the main paper. We select a representative scenario to illustrate the details of the *predict-then-optimize* pipeline in PLS operation, validating the overall solution in terms of both prediction accuracy and downstream optimization performance. The arrival information is chosen from Task 1, as shown in Table D.4. From the 400-day test set, we select Day 286, which exhibits the largest cost difference between DFL and SBL among the samples where DFL's MAE (Price) and MAE (Net Load) are both worse than SBL's, to showcase the differences in prediction and optimization between the two methods.

Appendix E.1. Dataset Analysis

Figure E.7 illustrates the statistical characteristics of electricity price, PV generation, and residential load in the dataset. The day-ahead electricity price exhibits a long-tailed distribution with occasional extreme values, indicating significant market volatility. Residential load follows a near-unimodal distribution with slight right skewness, centered around approximately 20 MW, reflecting a stable yet variable consumption pattern. In contrast, PV generation is highly concentrated near zero despite filtering for daytime hours (6:00-18:00), exhibiting a long positive tail.

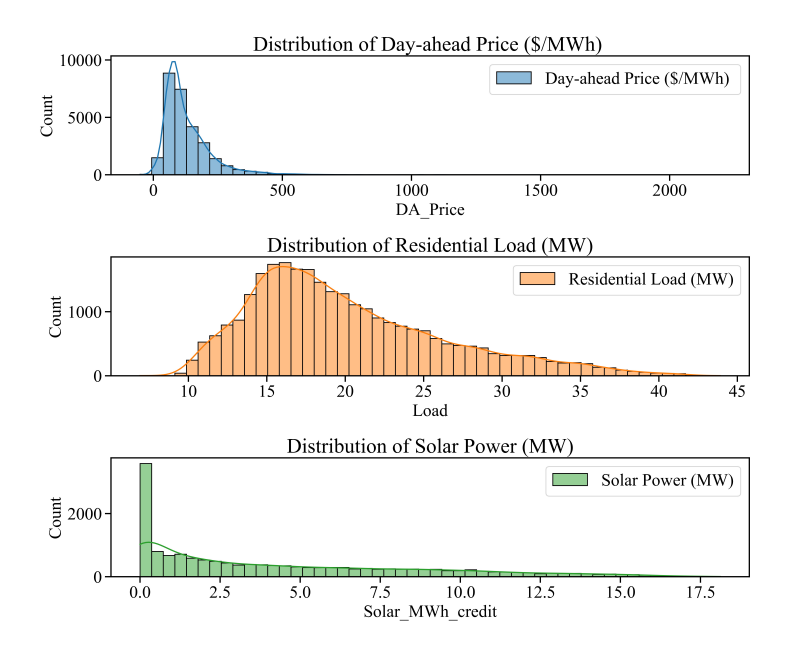


Figure E.7: Statistical characteristics of electricity price, PV generation, and residential load in the test set.

Figures E.8, E.9, and E.10 illustrate the time series trends of electricity price, load, and PV generation in the test set, respectively. The electricity price does not exhibit clear seasonal patterns and is non-stationary over the long term, with occasional extreme spikes. In contrast, both load and PV generation time series display pronounced seasonality.

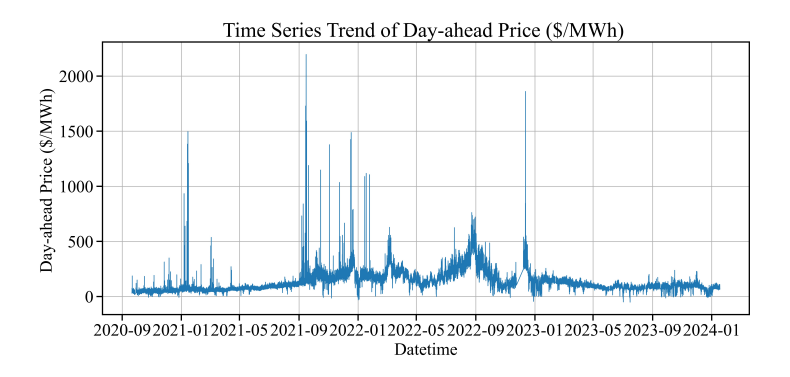


Figure E.8: Time series trend of electricity price in the test set.

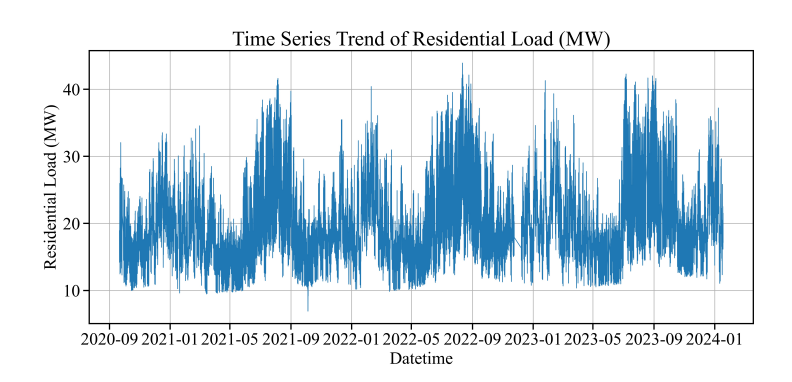


Figure E.9: Time series trend of load in the test set.

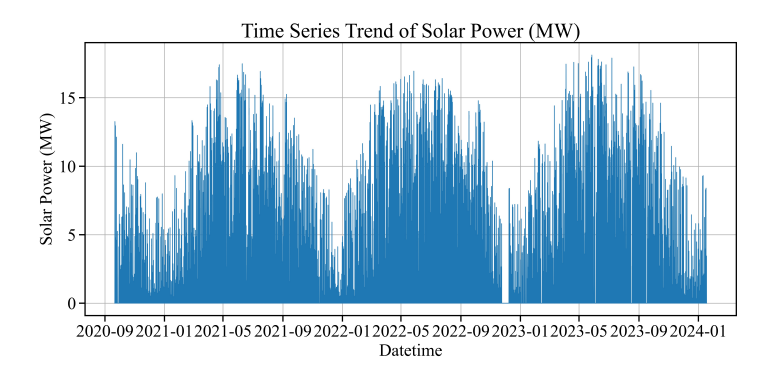


Figure E.10: Time series trend of PV generation in the test set. $\,$

Figures E.11 and E.12 present daily fluctuation box plots of electricity price and load in the dataset,

respectively. Both variables exhibit bimodal characteristics; however, electricity price demonstrates more pronounced volatility with a larger variance.

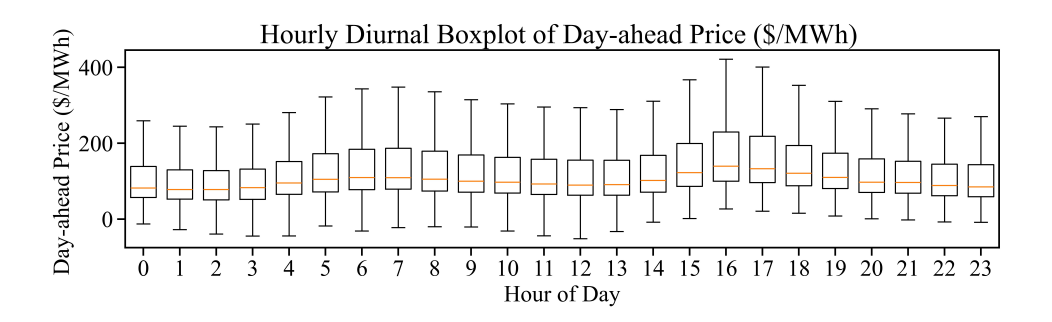


Figure E.11: Daily fluctuation box plot of electricity price in the dataset.

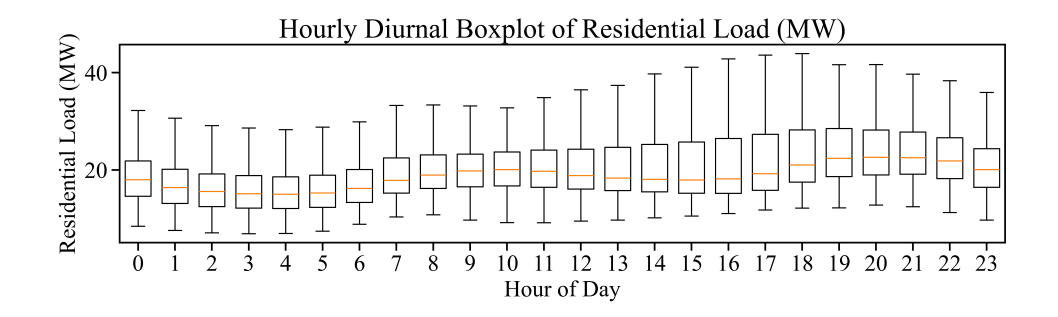


Figure E.12: Daily fluctuation box plot of load in the dataset.

Appendix E.2. Qualitative Visualization of Prediction Results

Figure E.13 illustrates the predicted electricity price and net load profiles for Day 286. Both the DFL and SBL models are able to capture the overall temporal dynamics of the net load with reasonable accuracy. In particular, the SBL demonstrates slightly superior performance in tracking the overall trajectory, whereas the DFL exhibits minor deviations at several time intervals, indicating a higher sensitivity to local fluctuations. Regarding price forecasting, both models achieve comparable accuracy, successfully reproducing the bimodal pattern observed in the actual price series. These results indicate that the proposed DFL framework is capable of maintaining satisfactory predictive performance across both price and net load forecasting tasks.

Appendix E.3. Qualitative Visualization of Cost Outcomes

The hourly operating cost and total vessel charging power schedule under the predicted electricity price and net-load profiles for Day 286 are illustrated in Fig. E.14. A key difference can be observed between

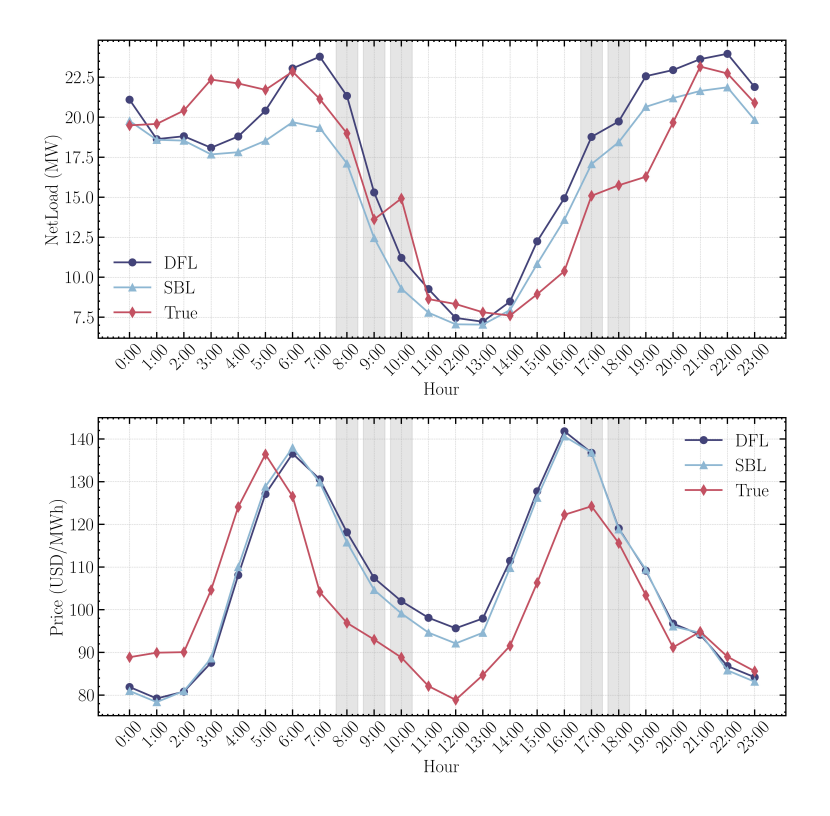


Figure E.13: Electricity price and net load predictions for Day 286. The gray shaded areas indicate time periods where DFL and SBL exhibit differences in operational costs at the current time.

08:00 and 10:00, during which the net-load curve exhibits a distinct inflection caused by variations in PV generation, leading to an underestimation of the actual net load. In this period, the DFL-based prediction demonstrates higher accuracy, resulting in a more reasonable vessel charging schedule that avoids excessive charging. Overall, the charging schedules of DFL and SBL remain similar during other hours; however, the improved accuracy of DFL at critical moments leads to a lower total operating cost. It should be noted that this analysis is case-specific, as the optimization decisions are highly sensitive to the entire curve profile yet the discussion is based on a single time slice. Nevertheless, the results highlight the importance of prediction accuracy at critical periods for achieving cost-effective operational decisions.

Appendix E.4. Qualitative Visualization of Power Dispatch Results

Figures E.15 and E.16 illustrate the scheduling results of various resources within the PLS during the day-ahead and real-time stages, respectively, obtained using the proposed DFL method. It can be observed that both the energy storage system and logistics loads are dispatched in a well-coordinated manner, and the total power output aligns with the bidding power in the day-ahead market. The energy storage system discharges during periods of high electricity price and charges during periods of low electricity price, thereby performing price arbitrage according to market variations. The logistics loads are primarily scheduled during

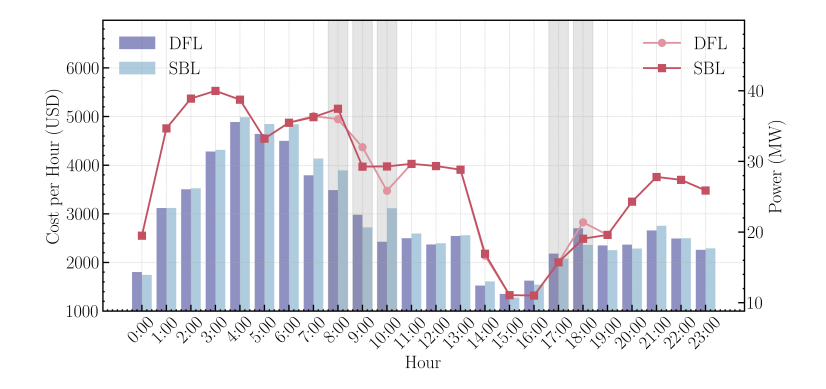


Figure E.14: Hourly operating cost and total vessel charging power schedule for Day 286. The gray shaded areas indicate time periods where DFL and SBL exhibit differences in operational costs at the current time. The bars represent the operating cost (left axis), while the lines depict the total charging power allocated to all vessels at the current time (right axis).

low-price periods to minimize operational costs, while their consumption is reduced as much as possible during high-price periods. Overall, the PLS effectively leverages the flexibility of both energy storage and logistics resources to respond to electricity market price fluctuations to achieve cost-efficient operation.

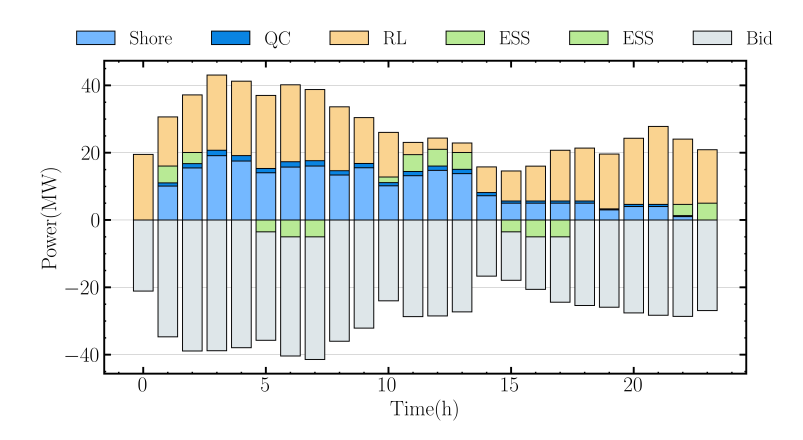


Figure E.15: Resource scheduling results in the PLS during the day-ahead stage for Day 286 using the DFL method. The stacked bars of different colors represent the power output of different resources, with negative bars indicating the discharge power of the energy storage and power purchased from the day-ahead market.

Appendix E.5. Quantitative Results on Logistics Scheduling

Figure E.17 presents the detailed vessel scheduling results of the PLS on Day 286. Overall, the DFL-based approach produces a reasonable allocation of berthing and loading-unloading tasks while satisfying all operational constraints. The berth assignments are appropriate, with the total occupied berth length at each time slice remaining within the available quay length, ensuring no berth conflicts. The in-port durations of all vessels meet their minimum loading-unloading time requirements. In terms of waiting time,

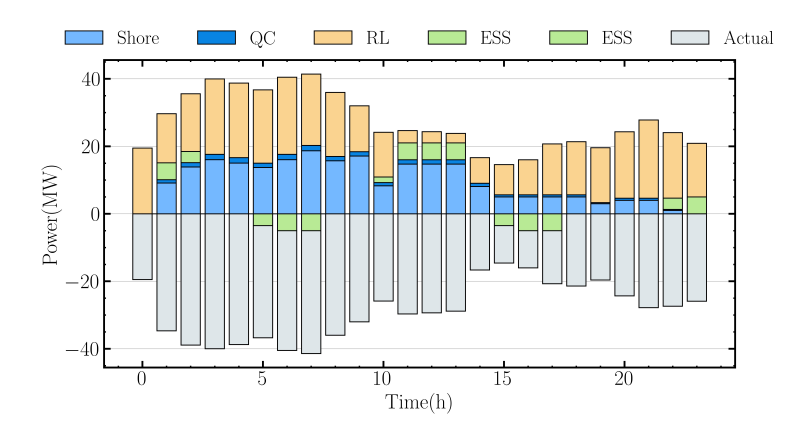


Figure E.16: Resource scheduling results in the PLS during the real-time stage for Day 286 using the DFL method. The stacked bars of different colors represent the power output of different resources, with negative bars indicating the discharge power of the energy storage and power purchased from outside power grid.

all vessels experience delays shorter than their maximum allowable limits, and most vessels have relatively short waiting periods.

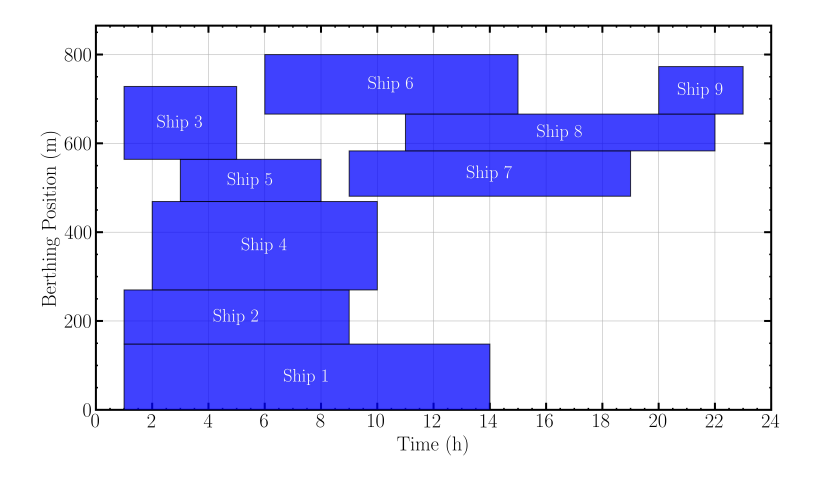


Figure E.17: Vessel scheduling results in the PLS for Day 286 using the DFL method. The blue rectangles represent vessels, with the length of each rectangle indicating the berthing duration, the width representing the vessel length, and the vertical position of the rectangle's bottom edge indicating the berth location. This figure illustrates the berth allocation and berthing time arrangements for all vessels throughout the operational day.

Figure E.18 illustrates the quay crane scheduling results for the same day. A total of ten quay cranes are deployed without any operational conflicts, and the number of cranes assigned at each time step stays within the minimum and maximum limits required by each vessel. Each quay crane services only one vessel at any given time, satisfying the operational constraints. It is also observed that quay crane operations are concentrated during periods of low electricity prices, demonstrating the rational responsiveness of logistics scheduling to electricity price variations within the PLS.

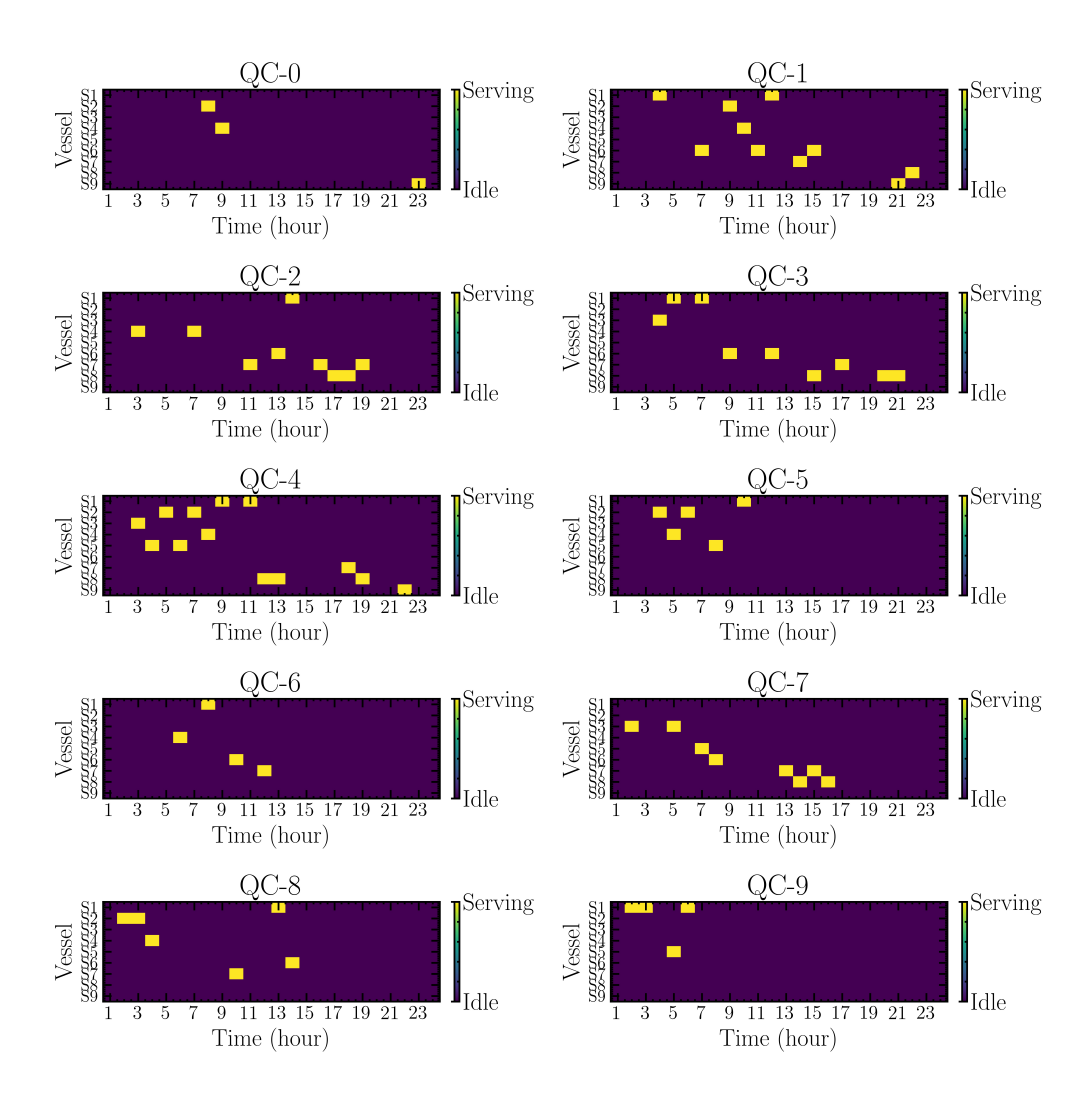


Figure E.18: Quay crane scheduling results in the PLS for Day 286 using the DFL method. Each subplot corresponds to the operational status of a different quay crane. The horizontal axis represents time, while the vertical axis denotes different vessels. A highlighted pixel in a subplot indicates that the corresponding quay crane is servicing vessel $j \leq$ total number of vessels at time $t \leq T$. Since each quay crane services only one vessel at any given time, each column along the time axis in a subplot contains at most one highlighted pixel.